Journal of Computational Physics 228 (2009) 1–32

Contents lists available at ScienceDirect

Journal of Computational Physics

journal homepage: www.elsevier.com/locate/jcp

A mass, energy, vorticity, and potential enstrophy conserving lateral fluid–land boundary scheme for the shallow water equations

G.S. Ketefian *, M.Z. Jacobson

Department of Civil and Environmental Engineering, Yang and Yamazaki Environment and Energy Building, Stanford University, Stanford, CA 94305-4020, United States

ARTICLE INFO

Article history:
Received 7 September 2007
Received in revised form 31 July 2008
Accepted 5 August 2008
Available online 23 August 2008

Keywords:
Shallow water equations
Boundary conditions
Conservation
Energy
Vorticity
Potential enstrophy

ABSTRACT

A numerical scheme for treating fluid–land boundaries in inviscid shallow water flows is derived that conserves the domain-summed mass, energy, vorticity, and potential enstrophy in domains with arbitrarily shaped boundaries. The boundary scheme is derived from a previous scheme that conserves all four domain-summed quantities only in periodic domains without boundaries. It consists of a method for including land in the model along with evolution equations for the vorticity and extrapolation formulas for the depth at fluid–land boundaries. Proofs of mass, energy, vorticity, and potential enstrophy conservation are given. Numerical simulations are carried out demonstrating the conservation properties and accuracy of the boundary scheme for inviscid flows and comparing its performance with that of four alternative boundary schemes. The first of these alternatives extrapolates or finite-differences the velocity to obtain the vorticity at boundaries; the second enforces the free-slip boundary condition; the third enforces the super-slip condition; and the fourth enforces the no-slip condition. Comparisons of the conservation properties demonstrate that the new scheme is the only one of the five that conserves all four domain-summed quantities, and it is the only one that both prevents a spurious energy cascade to the smallest resolved scales and maintains the correct flow orientation with respect to an external forcing. Comparisons of the accuracy demonstrate that the new scheme generates vorticity fields that have smaller errors than those generated by any of the alternative schemes, and it generates depth and velocity fields that have errors about equal to those in the fields generated by the most accurate alternative scheme.

© 2008 Elsevier Inc. All rights reserved.

1. Introduction

The use of energy, enstrophy, and/or potential enstrophy conserving numerical schemes for the solution of the governing equations of fluid flow has long been recognized as an effective means of eliminating nonlinear instabilities, controlling the accumulation of truncation errors in the smallest resolved scales, and reducing biases in the flow statistics in long-term simulations. Arakawa [1] first demonstrated that the use of an energy and enstrophy conserving scheme for the barotropic vorticity equation for 2D nondivergent flows eliminates nonlinear instabilities that are often present when non-conserving schemes are used. In doing so, he derived both a spatially second-order and a fourth-order accurate energy and enstrophy conserving scheme. Sadourny [2] compared an energy conserving scheme for the shallow water equations (henceforth SWEs) with a potential enstrophy conserving scheme and demonstrated that the latter simulated the energy cascade much more accurately than the former. Arakawa and Lamb [3] extended the second-order scheme of Arakawa [1] to the SWEs and to the 3D hydrostatic equations of the atmosphere. In a later study [4], they developed a scheme for the SWEs that conserves

* Corresponding author.
E-mail addresses: gsk@stanford.edu (G.S. Ketefian), jacobson@stanford.edu (M.Z. Jacobson).

0021-9991/$ - see front matter © 2008 Elsevier Inc. All rights reserved.
doi:10.1016/j.jcp.2008.08.009

both energy and potential enstrophy and demonstrated its advantages over a scheme that conserves energy for the SWEs but conserves enstrophy only for 2D nondivergent flows. (Note that when the fluid depth is held constant, the SWEs reduce to the equations for 2D nondivergent flow, and the potential enstrophy reduces to the enstrophy divided by the constant fluid depth.) To improve on the second-order accuracy of the energy and potential enstrophy conserving scheme of Arakawa and Lamb [4] (henceforth the AL81 scheme), Takano and Wurtele [5] developed a pseudo-fourth-order extension. (A pseudo-fourth-order scheme is one which, in the special case of 2D nondivergent flow, is fourth-order accurate in space; see, e.g. [6].) Abramopoulos [6] used operator formalism to derive second-order and pseudo-fourth-order energy and potential enstrophy conserving schemes for the SWEs on A-, B-, and C-grids. (For a description of the A- through E-grids, see, for instance, [3].) Later, Abramopoulos [7] derived a pseudo-fourth-order energy and enstrophy (but not potential enstrophy) conserving scheme for the SWEs that is a generalization of Arakawa's [1] fourth-order scheme for 2D nondivergent flows. Tripoli [8] demonstrated the superiority of an enstrophy conserving scheme applied to nonhydrostatic atmospheric flows relative to higher order non-conserving schemes.

The schemes cited above (except some of the ones in [6]) are all implemented on the fully staggered Arakawa C-grid. Other researchers have focused on the E-grid. Janjić [9] derived a second-order energy and enstrophy conserving scheme for 2D nondivergent flows on the semi-staggered E-grid. Mesinger [10] generalized the scheme of Janjić [9] to conserve energy for divergent flows (i.e. the SWEs) with the equations expressed in rotational or vector-invariant form (as in this paper). He also derived an approximately fourth-order counterpart of this generalized scheme, again on the E-grid. Janjić [11] showed that conservation of energy and enstrophy as defined on the E-grid does not guarantee the prevention of a false energy cascade to small scales. To overcome this problem, he derived an E-grid scheme for 2D nondivergent flows that conserves energy and enstrophy as defined on the C-grid and then generalized it to the SWEs. Rančić [12] generalized the scheme of Janjić [11] to pseudo-fourth-order.

Energy, enstrophy, and/or potential enstrophy conserving schemes have also been derived on non-rectangular and irregular grids. Sadourny et al. [13] derived a finite-difference scheme for the barotropic vorticity equation for 2D nondivergent flows on an icosahedral–hexagonal grid covering the sphere. Salmon and Talley [14] generalized Arakawa's energy and enstrophy conserving discretization of the Jacobian [1] to include not only finite-difference methods but also spectral and finite-element methods (with the latter allowing for irregular grids such as triangles). More recently, Perot [15] derived discretizations of both the flux and rotational forms of the incompressible Navier–Stokes equations on unstructured grids. The discretization of the flux form conserves mass, momentum, and kinetic energy and the one of the rotational form conserves mass, kinetic energy, and vorticity (but neither conserves enstrophy or potential enstrophy). Morton and Roe [16] derived a mass, momentum, and vorticity (but not energy, enstrophy, or potential enstrophy) conserving scheme for the linearized equations of motion on unstructured grids. However, since they only consider the linearized equations, their scheme does not specify how to treat the nonlinear terms. Ringler and Randall [17,18] developed an energy and potential enstrophy conserving scheme on hexagonal geodesic grids, both for the momentum formulation and the vorticity-divergence formulation of the SWEs. In part to avoid the computational modes encountered by Ringler and Randall [17,18], Bonaventura and Ringler [19] developed energy or potential enstrophy conserving schemes on Delaunay triangles using C-grid staggering (i.e. mass points located at triangle centers and velocities located on faces). Salmon [20–22] has employed a novel approach to derive mass, energy, vorticity, and potential enstrophy conserving schemes for the SWEs. In [20], he casts the equations in terms of Poisson brackets to derive a general algorithm that can be used to generate a variety of conserving schemes, including those of Arakawa and Lamb [4] and Takano and Wurtele [5]. In [21,22], he recasts the SWEs (in addition to other dynamical systems in [21]) in terms of Nambu brackets. He then shows that any numerical scheme for the SWEs (e.g. finite-difference, finite-element, and spectral) that maintains the antisymmetry property of the Nambu bracket will conserve energy and potential enstrophy. (The specific finite-difference schemes derived in [22] also conserve mass and circulation, the latter being the domain integral of the vorticity.) One potential drawback of the schemes in [22] is their need to solve elliptic equations at each time step.

An important aspect of these quadratically conservative schemes that has apparently not been studied in much detail is their application to domains with arbitrarily shaped boundaries, e.g. domains with embedded islands. (Domains that encompass islands are often referred to as multiply connected domains.) Such domains are unavoidable in both 2D and 3D ocean models and in 3D atmospheric models using vertical coordinates that intersect the topography (e.g. the altitude coordinate). In our literature review, we have found only a few instances in which quadratically conservative schemes have been modified (from their usual forms within the flow) to account for the presence of lateral boundaries in such a way that maintains, or at least attempts to maintain, all of the conservation properties. Arakawa [1] presented a modification of his energy and enstrophy conserving scheme for 2D nondivergent flow to account for flat walls (but not corners). Salmon and Talley [14] extended the work of Arakawa [1] to include concave and convex corners and boundaries situated at arbitrary angles. In order to adapt the E-grid energy and enstrophy conserving scheme of Janjić [11] to a 3D hydrostatic atmospheric model that uses the step-mountain η vertical coordinate – a coordinate that intersects the topography – Mesinger et al. [23] presented a scheme to take into account lateral boundaries. In this boundary scheme, the no-slip (along with the no-flux) condition is enforced. Note, however, that the no-slip boundary condition is not consistent with the equations for inviscid 2D nondivergent flow; it is an over specification. Mesinger et al. [23] do not show results for purely 2D nondivergent inviscid flow in domains with arbitrary boundaries; they only show results from their full 3D model, which includes a boundary layer parameterization. Thus, it is difficult to evaluate the performance of their boundary scheme. Adcroft et al. [24] have used shaved cells to improve the representation of the bathmetry in a 3D incompressible ocean model. The finite-volume approach they use conserves mass, momentum, and energy but not vorticity, enstrophy, or potential enstrophy. Finally, Salmon

[22] states that his mass, energy, vorticity, and potential enstrophy conserving scheme for the SWEs can easily account for lateral boundaries by dropping "the terms arising from grid boxes that lie outside boundaries". However, as in [23], no results are shown from numerical simulations in domains with arbitrary boundaries.

With very few exceptions, shallow water models that simulate flows in domains with lateral fluid–land boundaries use either harmonic or biharmonic dissipation (e.g. [25–32]). In some instances, this dissipation is physically justified, and in others, it is necessary for numerical stability and/or to remove grid-scale numerical noise. We have found only four studies in which the purely inviscid SWEs are solved in domains with lateral boundaries. These consist of the original work of Arakawa and Lamb [4] that introduced the AL81 scheme and more recent works by Evans et al. [33], Hart and Evans [34], and Mundt et al. [35]. None of these studies simulates flows in domains with arbitrary boundaries as we do here. All four use the AL81 scheme to simulate zonal channel flow, i.e. flow with periodic boundary conditions in the zonal and rigid wall (i.e. no-flux) boundaries in the meridional. As described in Section 6, the AL81 scheme requires specification of the potential vorticity at the channel walls. For this purpose, Arakawa and Lamb [4] use the free-slip condition (in which the relative vorticity on the boundary is set to zero) to specify the potential vorticity at the channel walls, although they do not specify how they calculate the height at the walls (this being necessary in order to calculate the potential vorticity in the presence of the Coriolis effect). The other three studies [33–35] seem to have used this same free-slip condition. We will show in Section 8.1 that the free-slip condition does not conserve domain-summed vorticity and thus is not the optimal method of treating the boundaries, although it is better than some other methods.

In this paper, we derive and implement a fluid–land boundary scheme that generalizes the mass, energy, vorticity, and potential enstrophy conserving AL81 scheme for the inviscid SWEs to domains with arbitrarily shaped boundaries. Our motivation for deriving such a scheme is to be able to construct a 3D nonhydrostatic global-to-urban scale atmospheric model that uses the height coordinate z and that discretizes the governing equations using the AL81 scheme. We intend to apply the new boundary scheme at the intersections of the model levels with the topography. In this way, we hope to eliminate spurious sources and sinks of energy, vorticity, and potential enstrophy that might otherwise arise at these intersections. The first step in constructing such a 3D atmospheric model is to derive and test a boundary scheme that works well for the simpler case of the SWEs. This is what we do here.

To maintain mass and energy conservation in the SWEs, we use a stair-step method of including land in the model and enforce the no-flux condition at boundaries. To maintain vorticity and potential enstrophy conservation, we derive a method for calculating the potential vorticity $q = \zeta/h$ at fluid–land boundaries (where ζ is the vorticity and h the fluid depth) that consists of solving an evolution equation for ζ and using an extrapolation formula to obtain h. We then perform numerical simulations demonstrating the conservation properties and accuracy of this boundary scheme in domains with arbitrary boundaries and compare it with several alternative boundary schemes for the SWEs.

Ideally, we would have liked to derive a piecewise linear or shaved-cell approach similar to the one presented by Adcroft et al. [24] to approximate boundaries. We attempted this but were unable to derive a scheme on shaved cells that conserves all four quantities. It seems that the natural method of including boundaries in the AL81 scheme is to locate them along curves on which the spatial variables (e.g. x and y) are constant. This in turn leads to the stair-step approach we present here (see Section 4). Fortunately, this is more than adequate for our purposes. For instance, it does not produce any of the numerical noise that Adcroft et al. [24] encounter with their stair-step scheme.

2. Shallow water equations

The SWEs for flow on a flat plane or on the surface of a sphere can be expressed in 2D orthogonal curvilinear coordinates (ξ, η) as follows (see [36]):

$$\frac{\partial}{\partial t}\left(\frac{h}{mn}\right) + \frac{\partial}{\partial \xi}\left(\frac{hu_\xi}{n}\right) + \frac{\partial}{\partial \eta}\left(\frac{hu_\eta}{m}\right) = 0 \tag{1}$$

$$\frac{\partial}{\partial t}\left(\frac{u_\xi}{m}\right) - \frac{hu_\eta}{m} q = -\frac{\partial}{\partial \xi}(K + \Phi) \tag{2}$$

$$\frac{\partial}{\partial t}\left(\frac{u_\eta}{n}\right) + \frac{hu_\xi}{n} q = -\frac{\partial}{\partial \eta}(K + \Phi) \tag{3}$$

(1) is the continuity equation, and (2) and (3) are the rotational or vector-invariant forms of the momentum equations [10,15]. h is the depth of the fluid layer, and u_ξ and u_η are the layer-averaged velocity components along curves of constant η and ξ, respectively, on the plane or sphere on which the flow evolves. q, K, and Φ are the potential vorticity, the kinetic energy per unit mass, and the geopotential, respectively, defined as $q = \zeta/h$, $K = (u_\xi^2 + u_\eta^2)/2$, and $\Phi = g(h + h_{\text{bot}})$. Here, ζ is the absolute vorticity, given by

$$\zeta = f + \zeta_{\text{rel}} \tag{4}$$

where f is the Coriolis parameter and ζ_{rel} is the relative vorticity, given by

$$\zeta_{\text{rel}} = mn\left[\frac{\partial}{\partial \xi}\left(\frac{u_\eta}{n}\right) - \frac{\partial}{\partial \eta}\left(\frac{u_\xi}{m}\right)\right] \tag{5}$$

Also, $g = 9.81\ \mathrm{m\ s^{-2}}$ is the gravitational acceleration, and $h_{\mathrm{bot}}(\xi,\eta)$ is the height of the bottom boundary measured from a reference surface. Finally, m and n are the inverse scale factors in the ξ and η directions, respectively. They are defined as follows. For a small change $\mathrm{d}\xi$ in the ξ coordinate, m is the ratio of $\mathrm{d}\xi$ to the corresponding change in physical distance $\mathrm{d}s_\xi$ along a curve of constant η, i.e. $m = \mathrm{d}\xi/\mathrm{d}s_\xi$. Similarly, $n = \mathrm{d}\eta/\mathrm{d}s_\eta$, where $\mathrm{d}s_\eta$ is the change in physical distance along a curve of constant ξ corresponding to a change $\mathrm{d}\eta$ in the η coordinate. For example, in Cartesian coordinates $(\xi,\eta) = (x,y),\ m = n = 1$; in cylindrical coordinates $(\xi,\eta) = (r,\theta),\ m = 1$ and $n = 1/r$; and in spherical coordinates $(\xi,\eta) = (\lambda,\phi),\ m = 1/(a\cos\phi)$ and $n = 1/a$ (where λ is longitude, ϕ is latitude, and a is the radius of the sphere on which the flow evolves).

We take (1)–(3) to be valid in a rectangular domain Ω in the $\xi\eta$ plane bounded by $\xi = \xi_{\min},\ \xi = \xi_{\max},\ \eta = \eta_{\min}$, and $\eta = \eta_{\max}$. The boundary conditions on the outer edges of this domain can be periodic, no-flux, or a combination of the two. Ω is in general multiply connected, i.e. it can encompass land bodies of arbitrary shape (although these land bodies are not part of Ω). The condition that must be enforced at the boundaries of these land bodies is no-flux.

We can use (1)–(3) to derive the following evolution equations for the energy TE (where the "T" stands for "total", since we are considering the sum of the kinetic and potential energies), vorticity ζ, potential vorticity q, and potential enstrophy r:

$$\frac{\partial}{\partial t}(\mathrm{TE}) + \frac{\partial}{\partial \xi}\left[\frac{hu_\xi}{n}(K+\Phi)\right] + \frac{\partial}{\partial \eta}\left[\frac{hu_\eta}{m}(K+\Phi)\right] = 0 \tag{6}$$

$$\frac{\partial}{\partial t}\left(\frac{\zeta}{mn}\right) + \frac{\partial}{\partial \xi}\left(\frac{u_\xi}{n}\zeta\right) + \frac{\partial}{\partial \eta}\left(\frac{u_\eta}{m}\zeta\right) = 0 \tag{7}$$

$$\frac{\partial q}{\partial t} + mu_\xi\frac{\partial q}{\partial \xi} + nu_\eta\frac{\partial q}{\partial \eta} = 0 \tag{8}$$

$$\frac{\partial}{\partial t}\left(\frac{r}{mn}\right) + \frac{\partial}{\partial \xi}\left(\frac{u_\xi}{n}r\right) + \frac{\partial}{\partial \eta}\left(\frac{u_\eta}{m}r\right) = 0 \tag{9}$$

Here, TE and r are given by

$$\mathrm{TE} = \frac{1}{2}\frac{h}{mn}\left[(u_\xi^2 + u_\eta^2) + g(h + h_{\mathrm{bot}})\right]; \quad r = \frac{1}{2}\frac{\zeta^2}{h} \tag{10}$$

Since the advective terms in (1), (6), (7) and (9) are in flux form, their integrals over Ω vanish. This is true for both periodic and no-flux boundary conditions along the outer edges of Ω and whether or not land bodies are present. Thus, the SWEs conserve the domain integrals of mass, energy, vorticity, and potential enstrophy.

3. Spatial discretization without land

We will use the AL81 scheme to discretize the SWEs away from fluid–land boundaries. This scheme uses the staggered Arakawa C-grid. The grid spacings $\Delta\xi$ and $\Delta\eta$ are given by $\Delta\xi = (\xi_{\max} - \xi_{\min})/I$ and $\Delta\eta = (\eta_{\max} - \eta_{\min})/J$, where I and J are the number of grid points in the ξ and η directions, respectively. On the C-grid, the depth h is defined at coordinates (ξ_i,η_j), abbreviated (i,j), where $\xi_i = \xi_{\min} + (i-1/2)\Delta\xi$ for $i = 1,\ldots,I$ and $\eta_j = \eta_{\min} + (j-1/2)\Delta\eta$ for $j = 1,\ldots,J$. For brevity, in the discrete equations we replace the velocity components u_ξ and u_η with u and v, respectively. u is defined at coordinates $(\xi_{i+1/2},\eta_j)$, abbreviated $(i+1/2,j)$, where $\xi_{i+1/2} = \xi_{\min} + i\Delta\xi$ for $i = 0,\ldots,I$. Similarly, v is defined at coordinates $(\xi_i,\eta_{j+1/2})$, abbreviated $(i,j+1/2)$, where $\eta_{j+1/2} = \eta_{\min} + j\Delta\eta$ for $j = 0,\ldots,J$. The vorticity ζ is defined at coordinates $(\xi_{i+1/2},\eta_{j+1/2})$, abbreviated $(i+1/2,j+1/2)$. We will refer to the locations (i,j) where h is defined as h-points, the locations $(i+1/2,j)$ where u is defined as u-points, the locations $(i,j+1/2)$ where v is defined as v-points, and the locations $(i+1/2,j+1/2)$ where ζ is defined as ζ-points.

First, we consider the continuity equation (1). The AL81 scheme discretizes this equation multiplied by $\Delta\xi\Delta\eta$ at h-points (i,j) as follows (see [4] or [36]):

$$\frac{\mathrm{d}}{\mathrm{d}t}(\Pi_{i,j}) = -[(\delta_\xi F) + (\delta_\eta G)]_{i,j} \tag{11}$$

Here, $\delta_\xi(\ldots)$ and $\delta_\eta(\ldots)$ are the differencing operators in the ξ and η directions, respectively [e.g. $(\delta_\xi F)_{i,j} = F_{i+1/2,j} - F_{i-1/2,j}$]. $\Pi_{i,j}$ is the mass (or, equivalently, the volume, since the fluid is assumed to have constant density) in a control volume consisting of the grid box centered at (i,j). We will refer to this control volume as an h-point control volume (or CV for short). Also, $F_{i-1/2,j}$ and $F_{i+1/2,j}$ are the mass fluxes in the ξ direction through the left and right faces of this CV, and $G_{i,j-1/2}$ and $G_{i,j+1/2}$ are the mass fluxes in the η direction through the lower and upper faces. $\Pi,\ F$, and G are given by

$$\Pi_{i,j} = (A^{(h)}h)_{i,j} \tag{12}$$

$$F_{i+1/2,j} = (\bar{h}^{\xi}u\,\Delta s_\eta)_{i+1/2,j} \tag{13}$$

$$G_{i,j+1/2} = (\bar{h}^{\eta}v\,\Delta s_\xi)_{i,j+1/2} \tag{14}$$

In (13) and (14), $\overline{(\ldots)}^{\xi}$ and $\overline{(\ldots)}^{\eta}$ are the averaging operators in the ξ and η directions, respectively [e.g. $\bar{h}^{\xi}_{i+1/2,j} = (h_{i+1j} + h_{ij})/2$], and Δs_ξ and Δs_η are the incremental distances in physical space corresponding to the grid spacings $\Delta\xi$ and $\Delta\eta$ in the $\xi\eta$ plane, i.e. $\Delta s_\xi = \Delta\xi/m$ and $\Delta s_\eta = \Delta\eta/n$. Also, $A^{(h)}$ is the horizontal area of the h-point CV, given by

$$A^{(h)}_{ij} = (\Delta s_\xi \Delta s_\eta)_{ij} = \frac{\Delta\xi}{m_{ij}} \frac{\Delta\eta}{n_{ij}} \tag{15}$$

Note that m and n are known functions of ξ and η. Thus, we can evaluate Δs_ξ and Δs_η at h-, u-, v-, and ζ-points as necessary.

We now consider the momentum equations (2) and (3). The AL81 scheme discretizes the ξ momentum equation (2) multiplied by $\Delta\xi$ at u-points $(i+1/2, j)$ and the η momentum equation (3) multiplied by $\Delta\eta$ at v-points $(i, j+1/2)$ as follows (see [36]):

$$\frac{\mathrm{d}}{\mathrm{d}t}(u\,\Delta s_\xi)_{i+1/2,j} = \left[\overline{\overline{G}^{\eta}\bar{q}^{\xi\eta}}^{\xi} + \frac{1}{48}\delta_\xi[(\delta_\eta G)(\delta_\xi\delta_\eta q)] - \frac{1}{12}\delta_\xi[\overline{F}^{\xi}(\delta_\eta\bar{q}^{\xi})] - \frac{1}{12}\overline{(\delta_\xi F)(\delta_\eta\bar{q}^{\xi})}^{\xi} - \delta_\xi(K+\Phi)\right]_{i+1/2,j} \tag{16}$$

$$\frac{\mathrm{d}}{\mathrm{d}t}(v\,\Delta s_\eta)_{ij+1/2} = \left[-\overline{\overline{F}^{\xi}\bar{q}^{\xi\eta}}^{\eta} - \frac{1}{48}\delta_\eta[(\delta_\xi F)(\delta_\xi\delta_\eta q)] + \frac{1}{12}\delta_\eta[\overline{G}^{\eta}(\delta_\xi\bar{q}^{\eta})] + \frac{1}{12}\overline{(\delta_\eta G)(\delta_\xi\bar{q}^{\eta})}^{\eta} - \delta_\eta(K+\Phi)\right]_{i,j+1/2} \tag{17}$$

In (16) and (17), Φ and K at h-points and q at ζ-points are given by

$$\Phi_{ij} = g(h + h_{\mathrm{bot}})_{ij} \tag{18}$$

$$K_{ij} = \left[\frac{1}{A^{(h)}}\frac{1}{2}\left(\overline{A^{(u)}u^2}^{\xi} + \overline{A^{(v)}v^2}^{\eta}\right)\right]_{ij} \tag{19}$$

$$q_{i+1/2,j+1/2} = \left(\frac{\zeta}{h^{(q)}}\right)_{i+1/2,j+1/2} \tag{20}$$

where the vorticity ζ and the interpolated depth $h^{(q)}$ are given at ζ-points by

$$\zeta_{i+1/2,j+1/2} = \left[f + \frac{1}{A^{(\zeta)}}\{\delta_\xi(v\,\Delta s_\eta) - \delta_\eta(u\,\Delta s_\xi)\}\right]_{i+1/2,j+1/2} \tag{21}$$

$$h^{(q)}_{i+1/2,j+1/2} = \left(\frac{\overline{\Pi}^{\xi\eta}}{A^{(\zeta)}}\right)_{i+1/2,j+1/2} \tag{22}$$

and the areas $A^{(u)}$, $A^{(v)}$, and $A^{(\zeta)}$ are given by

$$A^{(u)}_{i+1/2,j} = (\Delta s_\xi \Delta s_\eta)_{i+1/2,j} \tag{23}$$

$$A^{(v)}_{ij+1/2} = (\Delta s_\xi \Delta s_\eta)_{ij+1/2} \tag{24}$$

$$A^{(\zeta)}_{i+1/2,j+1/2} = \overline{(A^{(h)})}^{\xi\eta}_{i+1/2,j+1/2} \tag{25}$$

For periodic boundary conditions along the outer edges of Ω and without land, the AL81 scheme conserves the domain-summed mass, energy, vorticity, and potential enstrophy, i.e. (see [36])

$$\frac{\mathrm{d}}{\mathrm{d}t}(\mathrm{MASS}_{\mathrm{tot}}) = \frac{\mathrm{d}}{\mathrm{d}t}(\mathrm{TE}_{\mathrm{tot}}) = \frac{\mathrm{d}}{\mathrm{d}t}(\mathrm{VORT}_{\mathrm{tot}}) = \frac{\mathrm{d}}{\mathrm{d}t}(\mathrm{PENST}_{\mathrm{tot}}) = 0 \tag{26}$$

where

$$\mathrm{MASS}_{\mathrm{tot}} = \sum_{i=1}^{I}\sum_{j=1}^{J}\Pi_{ij} \tag{27}$$

$$\mathrm{TE}_{\mathrm{tot}} = \sum_{i=1}^{I}\sum_{j=1}^{J}\frac{1}{2}\left[\overline{A^{(u)}u^2\bar{h}^{\xi}}^{\xi} + \overline{A^{(v)}v^2\bar{h}^{\eta}}^{\eta} + g\Pi(h + 2h_{\mathrm{bot}})\right]_{ij} \tag{28}$$

$$\mathrm{VORT}_{\mathrm{tot}} = \sum_{i=1}^{I}\sum_{j=1}^{J}(A^{(\zeta)}\zeta)_{i+1/2,j+1/2} \tag{29}$$

$$\mathrm{PENST}_{\mathrm{tot}} = \sum_{i=1}^{I}\sum_{j=1}^{J}\left[A^{(\zeta)}\frac{1}{2}\frac{\zeta^2}{h^{(q)}}\right]_{i+1/2,j+1/2} \tag{30}$$

However, the AL81 scheme does not specify any method for treating no-flux boundaries, either along the outer edges of Ω or along the boundaries of internal land bodies. In the following sections, we present a no-flux boundary scheme that allows for the presence of land while maintaining the conservation properties (26).

4. Inclusion of land and mass conservation

We will include land in the model by designating each h-point CV as consisting entirely of either fluid or land. Note that this is a stair-step approach of approximating fluid–land boundaries. With this approach, we can place land CVs at arbitrary locations in order to approximate land bodies of any shape (although for coding convenience, we exclude from our model the two fluid–land configurations shown in Fig. 2; see Appendix C). Fig. 1 gives an example of such an arbitrary distribution of fluid and land CVs. The white CVs in the figure represent fluid while the shaded ones represent land. In this approach, h-points will lie either completely within fluid or completely within land; they will not lie on boundaries. On the other hand, u-, v-, and ζ-points can lie within fluid, on boundaries, or within land. As in the continuous equations, in the discrete equations no physical quantities will be defined within land; they will be defined only within fluid or at boundaries. To enforce the no-flux condition, we set $u_{i+1/2,j}$ and $v_{i,j+1/2}$ at the boundaries to zero (i.e. we do not solve the momentum equations at boundary u-points and boundary v-points). Note that we can no longer use (13) and (14) for the mass fluxes at boundaries because these would require undefined values of h from within land. Instead, we will use

$$F_{i+1/2,j} = (h^{\text{bdy},\xi} u \Delta s_\eta)_{i+1/2,j} \quad \text{at boundary } u\text{-points} \tag{31}$$

$$G_{i,j+1/2} = (h^{\text{bdy},\eta} v \Delta s_\xi)_{i,j+1/2} \quad \text{at boundary } v\text{-points} \tag{32}$$

where $h^{\text{bdy},\xi}_{i+1/2,j}$ and $h^{\text{bdy},\eta}_{i,j+1/2}$ are approximations to the depth at boundaries obtained using values of h from within the flow. Since we will always set u and v in (31) and (32) to zero to enforce the no-flux condition, we do not need to determine the forms of $h^{\text{bdy},\xi}$ and $h^{\text{bdy},\eta}$. With u and v set to zero, (31) and (32) reduce to

$$F_{i+1/2,j} = 0 \quad \text{at boundary } u\text{-points} \tag{33}$$

$$G_{i,j+1/2} = 0 \quad \text{at boundary } v\text{-points} \tag{34}$$

Combining these with the definitions of the mass fluxes at fluid u- and v-points given by (13) and (14), we get

$$F_{i+1/2,j} = \begin{cases} (\bar{h}^{\xi} u \Delta s_\eta)_{i+1/2,j} & \text{at fluid } u\text{-points} \\ 0 & \text{at boundary } u\text{-points} \end{cases} \tag{35}$$

$$G_{i,j+1/2} = \begin{cases} (\bar{h}^{\eta} v \Delta s_\xi)_{i,j+1/2} & \text{at fluid } v\text{-points} \\ 0 & \text{at boundary } v\text{-points} \end{cases} \tag{36}$$

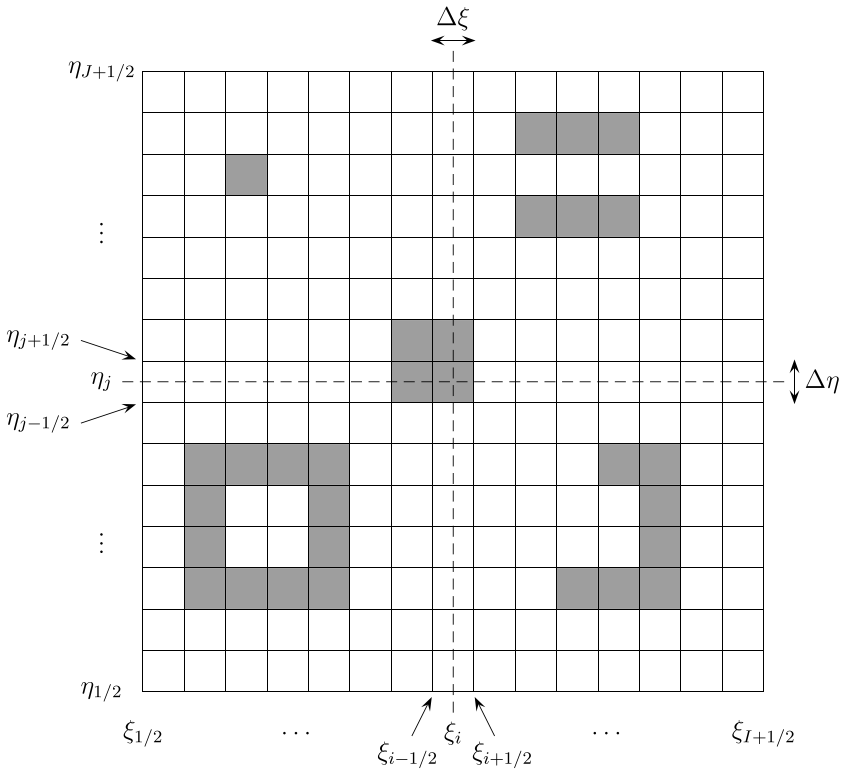

Fig. 1. Computational grid in the $\xi\eta$ plane showing an arbitrary mix of fluid and land control volumes (CVs). Each square represents an h-point CV having size $\Delta\xi$ in the ξ direction and $\Delta\eta$ in the η direction. The white CVs are fluid and the shaded CVs are land.

These are the general definitions of the mass fluxes in the presence of land.

We can obtain an evolution equation for the domain-summed mass by summing the discrete continuity equation (11) over all fluid h-points. Since F and G given by (35) and (36) satisfy the no-flux condition at fluid–land boundaries and since (11) is in flux form, the sum of the right-hand side (RHS) of (11) vanishes and we obtain

$$\frac{\mathrm{d}}{\mathrm{d}t}(\mathrm{MASS}_{\mathrm{tot}}) = 0 \tag{37}$$

where the domain-summed mass $\mathrm{MASS}_{\mathrm{tot}}$ is given by

$$\mathrm{MASS}_{\mathrm{tot}} = \sum_{\substack{\text{fluid} \\ h\text{-points}}} \Pi_{i,j} \tag{38}$$

Eq. (37) shows that $\mathrm{MASS}_{\mathrm{tot}}$ is conserved in the presence of land.

5. Energy conservation

We will now show that with the proper definition of the discrete energy at each fluid h-point, the method for including land in the flow domain presented in Section 4 conserves the domain-summed energy.

We define the total (i.e. kinetic plus potential) energy TE within any fluid h-point CV as

$$\mathrm{TE}_{i,j} = \mathrm{KE}_{i,j}^{(\xi)} + \mathrm{KE}_{i,j}^{(\eta)} + \mathrm{PE}_{i,j} \tag{39}$$

where $\mathrm{KE}^{(\xi)}$ and $\mathrm{KE}^{(\eta)}$ are the portions of the kinetic energy due to fluid motion in the ξ and η directions, respectively, and PE is the potential energy. These are given by

$$\mathrm{KE}_{i,j}^{(\xi)} = \frac{1}{2}\overline{(Fu\,\Delta s_\xi)}^{\xi}_{i,j}; \quad \mathrm{KE}_{i,j}^{(\eta)} = \frac{1}{2}\overline{(Gv\,\Delta s_\eta)}^{\eta}_{i,j}; \quad \mathrm{PE}_{i,j} = \frac{1}{2}[g\Pi(h + 2h_{\mathrm{bot}})]_{i,j} \tag{40}$$

We can obtain an evolution equation for TE by summing the evolution equations for $\mathrm{KE}^{(\xi)}$, $\mathrm{KE}^{(\eta)}$, and PE. The equation for $\mathrm{KE}^{(\xi)}$ can be obtained by multiplying the discrete momentum equation (16) by the mass flux F and averaging the result in the ξ direction. An analogous procedure can be used to obtain the equation for $\mathrm{KE}^{(\eta)}$. The equation for PE can be obtained by multiplying the discrete continuity equation (11) by Φ. After extensive algebra, we can show that the evolution equation for TE is given by

$$\frac{\mathrm{d}}{\mathrm{d}t}(\mathrm{TE}_{i,j}) = -[(\delta_\xi F^{\mathrm{TE}}) + (\delta_\eta G^{\mathrm{TE}})]_{i,j} \tag{41}$$

where F^{TE} and G^{TE} are the fluxes of energy in the ξ and η directions, given by

$$F_{i+1/2,j}^{\mathrm{TE}} = \begin{cases} \left[F(\overline{K}^{\xi} + \overline{\Phi}^{\xi}) - \frac{1}{4}F\left\{\delta_\xi(\overline{G}^{\eta}\overline{q}^{\xi\eta}) + \frac{1}{12}\overline{(\delta_\eta G)(\delta_\xi\delta_\eta q)}^{\xi}\right\} + \frac{1}{12}\overline{\left\{\overline{F^2}^{\xi} - \frac{1}{2}(\delta_\xi F)^2\right\}(\delta_\eta \overline{q}^{\xi})}^{\xi}\right. \\ \left. \quad -\frac{1}{8}u^2 A^{(u)}\delta_\xi\left(\frac{\mathrm{d}h}{\mathrm{d}t}\right)\right]_{i+1/2,j} & \text{at fluid } u\text{-points} \\ 0 & \text{at boundary } u\text{-points} \end{cases} \tag{42}$$

$$G_{i,j+1/2}^{\mathrm{TE}} = \begin{cases} \left[G(\overline{K}^{\eta} + \overline{\Phi}^{\eta}) + \frac{1}{4}G\left\{\delta_\eta(\overline{F}^{\xi}\overline{q}^{\xi\eta}) + \frac{1}{12}\overline{(\delta_\xi F)(\delta_\xi\delta_\eta q)}^{\eta}\right\} - \frac{1}{12}\overline{\left\{\overline{G^2}^{\eta} - \frac{1}{2}(\delta_\eta G)^2\right\}(\delta_\xi \overline{q}^{\eta})}^{\eta}\right. \\ \left. \quad -\frac{1}{8}v^2 A^{(v)}\delta_\eta\left(\frac{\mathrm{d}h}{\mathrm{d}t}\right)\right]_{i,j+1/2} & \text{at fluid } v\text{-points} \\ 0 & \text{at boundary } v\text{-points} \end{cases} \tag{43}$$

The tendency $(\mathrm{d}h/\mathrm{d}t)_{i,j}$ appearing in these fluxes can be obtained by substituting (12) into the discrete continuity equation (11). This gives

$$\frac{\mathrm{d}}{\mathrm{d}t}(h_{i,j}) = -\frac{1}{A_{i,j}^{(h)}}[(\delta_\xi F) + (\delta_\eta G)]_{i,j} \tag{44}$$

Note that we have not independently imposed the no-flux condition on the energy fluxes, i.e. we have not *defined* F^{TE} and G^{TE} to be zero at boundary u- and v-points, respectively. Rather, they automatically satisfy the no-flux condition. This is because the energy fluxes through fluid–land boundaries turn out to be proportional to the velocity components and mass fluxes through these boundaries (not shown). Since the latter two sets of quantities are zero due to the no-flux condition, the energy fluxes through fluid–land boundaries will also be zero.

To prove conservation of domain-summed energy, we sum (41) over all fluid h-points. Since (41) is in flux form and since F^{TE} and G^{TE} at fluid–land boundaries satisfy the no-flux condition, the sum of the RHS of (41) vanishes and we get

$$\frac{\mathrm{d}}{\mathrm{d}t}(\mathrm{TE}_{\mathrm{tot}}) = 0 \tag{45}$$

where the domain-summed energy TE_{tot} is defined as

$$TE_{tot} = \sum_{\substack{\text{fluid} \\ h\text{-points}}} TE_{i,j} \tag{46}$$

Eq. (45) shows that TE_{tot} is conserved in the presence of land. Note that this result is independent of the method used to calculate ζ, $h^{(q)}$, and q at boundary ζ-points. In Section 8.1, we will present numerical simulations demonstrating energy conservation in the presence of land.

6. Potential vorticity, vorticity, and fluid depth at boundaries

In order to evaluate the right-hand sides of the discrete momentum equations (16) and (17) at fluid u- and v-points that lie within one h-point CV of a boundary, we need values of q at ζ-points that lie on the boundary. We will still use (20) to obtain q from ζ and $h^{(q)}$ at boundary ζ-points, but we cannot use (21) and (22) to obtain ζ and $h^{(q)}$ because doing so would require undefined values of h, u, and v from within land. In this section, we derive a method for calculating ζ and $h^{(q)}$ at boundary ζ-points.

Since the AL81 scheme (in the absence of boundaries) conserves vorticity, it must be possible to express the discrete evolution equation for the vorticity at a fluid ζ-point in flux form. We will derive such an equation below. This equation applies to CVs of dimensions $\Delta\xi \times \Delta\eta$ in the $\xi\eta$ plane centered around each ζ-point. We will refer to these as ζ-point CVs (see Fig. 3). When land is included in the model using the stair-step approach described in Section 4, fluid–land boundaries cut through the full CVs centered at boundary ζ-points. (Here, by "full" CV we mean the CV that would be associated with a ζ-point if it lay completely in fluid. This always consists of the rectangle of dimensions $\Delta\xi \times \Delta\eta$ centered around the ζ-point.) Parts of the full CV will lie in fluid and the remainder will lie in land. As a result, the actual CV associated with a boundary ζ-point will consist of only those parts of its full CV that lie in fluid. With our stair-step approach of including land, these parts will come in quarters. Thus, the actual CV associated with the boundary ζ-point will consist of a quarter, half, or three-quarters of its full CV (see Fig. 4). The vorticity equation for AL81 will no longer apply to these boundary ζ-point CVs because it would require values of various quantities within land. Nevertheless, we can maintain vorticity conservation in the overall scheme if the discrete evolution equations associated with these boundary ζ-point CVs are in flux form. In these equations, the vorticity fluxes through fluid–land boundaries must be zero to satisfy the no-flux condition, and the fluxes through faces shared with neighboring ζ-point CVs must match (i.e. be equal in magnitude but opposite in sign) the fluxes through these same faces appearing in the vorticity equations for these neighbors. This suggests that instead of calculating the vorticity at boundaries using nearby velocity components (e.g. by finite-differencing or extrapolation), we should obtain it by solving flux-form vorticity evolution equations. This is in fact what we will do. This approach will not only conserve vorticity but it will also be consistent with the mathematical nature of the inviscid SWEs in the following sense. Besides the no-flux condition, there is no other boundary condition for the inviscid SWEs like there is for the viscous SWEs (which have the no-slip condition). Thus, an evolution equation for some quantity, e.g. the tangential velocity component or, in our case, the vorticity, must be solved at the boundary.

To obtain vorticity equations at boundary ζ-points that satisfy the above conservation requirements, we will first split the discrete vorticity equation for a fluid ζ-point CV (i.e. the flux-form vorticity equation for the AL81 scheme without land) into four equations, one for each quarter of the CV. We will do this such that the equation for each quarter is in flux form and such that the sum of these four equations yields back the vorticity equation for the full CV. We will then use as the vorticity equation at a boundary ζ-point the sum of the equations for only those quarters of the full CV that lie in fluid. These equations will be discrete counterparts of the continuous flux-form vorticity evolution equation (7), and they will of course be constructed such that they do not require values of any physical quantities within land.

In order to completely determine the forms of the boundary vorticity equations, in addition to vorticity conservation we will impose several other physical and mathematical constraints. These constraints will not only determine the forms of the boundary vorticity equations, but they will also yield extrapolation formulas for the depth $h^{(q)}$ at boundary ζ-points (which is needed in calculating $q = \zeta/h^{(q)}$). The constraints we will impose include reduction of the vorticity fluxes to zero in the limit as the grid spacings approach zero, exact advection of q on the boundary when it is uniform in the immediate neighborhood of the boundary, and exactness of the extrapolation formulas for $h^{(q)}$ in the special case in which the depth is uniform in the immediate neighborhood of the boundary.

Before deriving the boundary vorticity equations, it is useful to categorize the various fluid–land configurations that might be encountered at a boundary ζ-point. Note that every ζ-point on the computational grid is surrounded by four neighboring h-point CVs. Since in our stair-step approach of including land each h-point CV is either entirely fluid or entirely land, there are a total of $2^4 = 16$ possible fluid–land configurations around a given ζ-point. One of these consists of all four h-points being land. In this case, ζ, $h^{(q)}$, and q are all undefined and will not be used. Another configuration consists of all four h-points being fluid. In this case, we first use (21) and (22) to calculate ζ and $h^{(q)}$ and then use (20) to calculate q (i.e. the AL81 scheme). Another two correspond to the excluded configurations in Fig. 2, so we will not consider them here (although these can be included in the model at the expense of a more complicated computer code; see Appendix C). The remaining 12 configurations can be categorized into one of the following four boundary geometries:

(1) concave corners (4 configurations)
(2) horizontal walls (2 configurations)

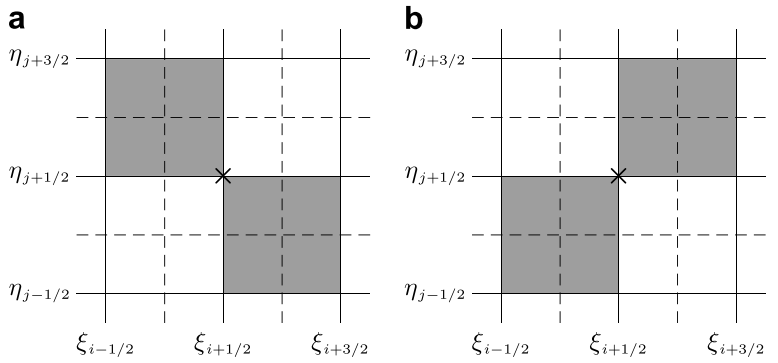

Fig. 2. The two fluid–land configurations excluded from the numerical model for coding convenience (see Appendix C). The white squares represent fluid h-point CVs while the shaded ones represent land. For each configuration, the "×" marks the location of the ζ-point at which the vorticity would have to be double-valued.

(3) vertical walls (2 configurations)
(4) convex corners (4 configurations)

Fig. 4 shows an example fluid–land configuration from each of these boundary geometries along with the ζ-point CV associated with each. The thick dashed line segments in the figure denote the boundaries of the CVs.

We begin the derivation of the vorticity equations at boundary ζ-points by deriving the discrete vorticity equation at a fluid ζ-point for the AL81 scheme without land. We can obtain this equation by taking $\delta_\xi(\ldots)$ of (17), subtracting from the result $\delta_\eta(\ldots)$ of (16), and using the definition of ζ given by (21). This gives the following flux-form evolution equation for the vorticity (as derived in detail in [36]):

$$\frac{\mathrm{d}}{\mathrm{d}t}(A^{(\zeta)}\zeta)_{i+1/2,j+1/2} = -[(\delta_\xi F^{(\zeta)}) + (\delta_\eta G^{(\zeta)})]_{i+1/2,j+1/2} \tag{47}$$

Expanding the differencing operators on the right-hand side gives

$$\frac{\mathrm{d}}{\mathrm{d}t}(A^{(\zeta)}\zeta)_{i+1/2,j+1/2} = -[(F^{(\zeta)}_{i+1,j+1/2} - F^{(\zeta)}_{ij+1/2}) + (G^{(\zeta)}_{i+1/2,j+1} - G^{(\zeta)}_{i+1/2,j})] \tag{48}$$

Here, $A^{(\zeta)}_{i+1/2,j+1/2}$ defined by (25) is the horizontal area associated with the CV of dimensions $\Delta\xi \times \Delta\eta$ in the $\xi\eta$ plane centered around the ζ-point at $(i+1/2, j+1/2)$, and $F^{(\zeta)}_{ij+1/2}$, $F^{(\zeta)}_{i+1,j+1/2}$, $G^{(\zeta)}_{i+1/2,j}$, and $G^{(\zeta)}_{i+1/2,j+1}$ are the vorticity fluxes through the faces of this CV. These fluxes are given by (see [36])

$$F^{(\zeta)}_{i,j+1/2} = \left[\overline{\overline{F}^{\xi}\bar{q}^{\xi}}^{\eta} - \frac{1}{12}\delta_\eta[\overline{F}^{\xi}(\delta_\eta \bar{q}^{\xi})] - \frac{1}{12}(\delta_\eta \overline{G}^{\eta})(\delta_\xi q)\right]_{i,j+1/2} \tag{49}$$

$$G^{(\zeta)}_{i+1/2,j} = \left[\overline{\overline{G}^{\eta}\bar{q}^{\eta}}^{\xi} - \frac{1}{12}\delta_\xi[\overline{G}^{\eta}(\delta_\xi \bar{q}^{\eta})] - \frac{1}{12}(\delta_\xi \overline{F}^{\xi})(\delta_\eta q)\right]_{i+1/2,j} \tag{50}$$

The ζ-point CV and the vorticity fluxes through its faces are shown in Fig. 3.

We now write the vorticity equations for the northwestern (NW), northeastern (NE), southwestern (SW), and southeastern (SE) quarters, respectively, of the fluid ζ-point CV centered at $(i+1/2, j+1/2)$ as follows:

$$\frac{\mathrm{d}}{\mathrm{d}t}(A^{(\zeta),\mathrm{NW}}\zeta)_{i+1/2,j+1/2} = -[(\widehat{F}^{(\zeta),\mathrm{N}} - F^{(\zeta),\mathrm{NW}}) + (G^{(\zeta),\mathrm{NW}} - \widehat{G}^{(\zeta),\mathrm{W}})]_{i+1/2,j+1/2} \tag{51}$$

$$\frac{\mathrm{d}}{\mathrm{d}t}(A^{(\zeta),\mathrm{NE}}\zeta)_{i+1/2,j+1/2} = -[(F^{(\zeta),\mathrm{NE}} - \widehat{F}^{(\zeta),\mathrm{N}}) + (G^{(\zeta),\mathrm{NE}} - \widehat{G}^{(\zeta),\mathrm{E}})]_{i+1/2,j+1/2} \tag{52}$$

$$\frac{\mathrm{d}}{\mathrm{d}t}(A^{(\zeta),\mathrm{SW}}\zeta)_{i+1/2,j+1/2} = -[(\widehat{F}^{(\zeta),\mathrm{S}} - F^{(\zeta),\mathrm{SW}}) + (\widehat{G}^{(\zeta),\mathrm{W}} - G^{(\zeta),\mathrm{SW}})]_{i+1/2,j+1/2} \tag{53}$$

$$\frac{\mathrm{d}}{\mathrm{d}t}(A^{(\zeta),\mathrm{SE}}\zeta)_{i+1/2,j+1/2} = -[(F^{(\zeta),\mathrm{SE}} - \widehat{F}^{(\zeta),\mathrm{S}}) + (\widehat{G}^{(\zeta),\mathrm{E}} - G^{(\zeta),\mathrm{SE}})]_{i+1/2,j+1/2} \tag{54}$$

In these, $A^{(\zeta),\mathrm{NW}}$, $A^{(\zeta),\mathrm{NE}}$, $A^{(\zeta),\mathrm{SW}}$, and $A^{(\zeta),\mathrm{SE}}$ are the areas associated with the quarters, and the quantities on the RHSs are the vorticity fluxes through the faces of these quarters. These are shown in Fig. 5. The forms of these areas and fluxes in terms of the dependent variables h, u, and v and other known quantities (such as the inverse scale factors m and n) are still to be determined.

Each of the eight quantities $F^{(\zeta),\mathrm{NW}}$, $F^{(\zeta),\mathrm{NE}}$, $F^{(\zeta),\mathrm{SW}}$, $F^{(\zeta),\mathrm{SE}}$, $G^{(\zeta),\mathrm{NW}}$, $G^{(\zeta),\mathrm{NE}}$, $G^{(\zeta),\mathrm{SW}}$, and $G^{(\zeta),\mathrm{SE}}$ in (51)–(54) represents a vorticity flux between one of the quarters of the ζ-point CV at $(i+1/2, j+1/2)$ and a quarter that is part of a neighboring ζ-point CV,

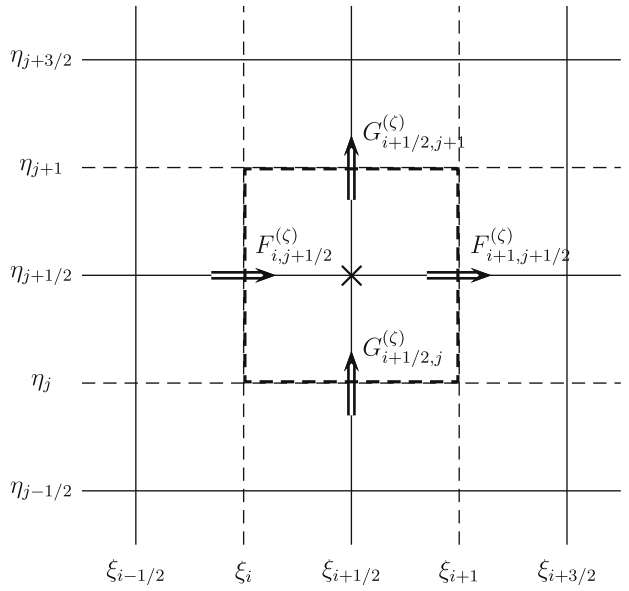

Fig. 3. A ζ-point control volume in the $\xi\eta$ plane that is completely within fluid. The thick dashed line segments denote the boundary of the CV, and the arrows denote the vorticity fluxes through this boundary. The "$\times$" marks the location of the ζ-point.

while each of the four quantities $\widehat{F}^{(\zeta),\mathrm{N}}$, $\widehat{F}^{(\zeta),\mathrm{S}}$, $\widehat{G}^{(\zeta),\mathrm{E}}$, and $\widehat{G}^{(\zeta),\mathrm{W}}$ represents a vorticity flux between two adjacent quarters of the ζ-point CV at $(i+1/2, j+1/2)$. For this reason, we will refer to the former set of fluxes as the external vorticity fluxes and the latter set as the internal fluxes. Note that (51)–(54) are written in flux form with respect to the internal fluxes, i.e. they are written such that when the equations for any two adjacent quarters are added, the vorticity flux between the two does not appear in the resulting equation. For example, the sum of (53) and (54) does not contain the flux $\widehat{F}^{(\zeta),\mathrm{S}}$. For this reason, the only situation in which the internal fluxes may appear in the vorticity equation for a boundary ζ-point is when these fluxes lie on a fluid–land boundary, and in that case they will be zero due to the no-flux boundary condition. Thus, the internal fluxes will never actually appear in the vorticity equations at boundaries. We will demonstrate this below for the case of a concave corner with fluid to the northwest.

To derive expressions for the external vorticity fluxes in (51)–(54) in terms of the dependent variables, first note that in order to conserve domain-summed vorticity, the vorticity fluxes out of boundary ζ-point CVs must match the corresponding fluxes into neighboring ζ-point CVs. This must be true whether these neighboring CVs are also boundary CVs or are fluid CVs. At faces shared by two boundary CVs, we can ensure that the vorticity flux out of one of these CVs equals the flux into the other by requiring that

$$F^{(\zeta),\mathrm{SW}}_{i+1/2,j+1/2} = F^{(\zeta),\mathrm{SE}}_{i-1/2,j+1/2} \tag{55}$$
$$G^{(\zeta),\mathrm{SW}}_{i+1/2,j+1/2} = G^{(\zeta),\mathrm{NW}}_{i+1/2,j-1/2} \tag{56}$$
$$F^{(\zeta),\mathrm{NW}}_{i+1/2,j+1/2} = F^{(\zeta),\mathrm{NE}}_{i-1/2,j+1/2} \tag{57}$$
$$G^{(\zeta),\mathrm{SE}}_{i+1/2,j+1/2} = G^{(\zeta),\mathrm{NE}}_{i+1/2,j-1/2} \tag{58}$$

At faces shared by a boundary and a fluid ζ-point CV, we can ensure that the vorticity flux out of the boundary CV equals the flux into the fluid CV by requiring that

$$(F^{(\zeta),\mathrm{NW}} + F^{(\zeta),\mathrm{SW}})_{i+1/2,j+1/2} = F^{(\zeta)}_{ij+1/2} \tag{59}$$
$$(F^{(\zeta),\mathrm{NE}} + F^{(\zeta),\mathrm{SE}})_{i+1/2,j+1/2} = F^{(\zeta)}_{i+1j+1/2} \tag{60}$$
$$(G^{(\zeta),\mathrm{SW}} + G^{(\zeta),\mathrm{SE}})_{i+1/2,j+1/2} = G^{(\zeta)}_{i+1/2,j} \tag{61}$$
$$(G^{(\zeta),\mathrm{NW}} + G^{(\zeta),\mathrm{NE}})_{i+1/2,j+1/2} = G^{(\zeta)}_{i+1/2,j+1} \tag{62}$$

where $F^{(\zeta)}$ and $G^{(\zeta)}$ are given by (49) and (50).

In order to uniquely determine the external vorticity fluxes in terms of the dependent variables, we need an additional set of constraints on their forms. We can derive this by noting that our boundary scheme will be applicable to arbitrary fluid–land configurations only if all quantities in the vorticity equation for a given ζ-point CV quarter that is within fluid are well-defined regardless of whether the three remaining quarters that make up the full CV at that ζ-point are within fluid or land. This implies that the equation for each quarter must involve only quantities (such as mass fluxes and potential vorticities) associated with the h-point CV to which the quarter belongs. For example, the equation for the northwestern quarter in Fig. 5

must involve only quantities within or on the faces of the h-point CV centered at $(i,j+1)$. Following this constraint, we now require that the expression for $F^{(\zeta),\mathrm{NW}}_{i+1/2,j+1/2}$ involve mass fluxes and potential vorticities evaluated only on or above the line $\eta=\eta_{j+1/2}$ and on or to the left of the line $\xi=\xi_{i+1/2}$ (see Fig. 5). Similarly, we require that the expression for $F^{(\zeta),\mathrm{SW}}_{i+1/2,j+1/2}$ involve mass fluxes and potential vorticities evaluated only on or below the line $\eta=\eta_{j+1/2}$ and on or to the left of the line $\xi=\xi_{i+1/2}$. We can obtain an expression for the sum of $F^{(\zeta),\mathrm{NW}}$ and $F^{(\zeta),\mathrm{SW}}$ by expanding some of the averaging and differencing operators on the RHS of (49) and substituting the result into the RHS of (59). This gives

$$F^{(\zeta),\mathrm{NW}}_{i+1/2,j+1/2}+F^{(\zeta),\mathrm{SW}}_{i+1/2,j+1/2}=\left[\left\{\overline{F}^{\xi}\left(\frac{1}{2}\bar{q}^{\xi\eta}-\frac{1}{12}(\delta_\eta\bar{q}^{\xi})\right)\right\}_{i,j+1}-\frac{1}{24}G_{i,j+3/2}(\delta_\xi q)_{i,j+1/2}\right]+\left[\left\{\overline{F}^{\xi}\left(\frac{1}{2}\bar{q}^{\xi\eta}+\frac{1}{12}(\delta_\eta\bar{q}^{\xi})\right)\right\}_{i,j}+\frac{1}{24}G_{i,j-1/2}(\delta_\xi q)_{i,j+1/2}\right] \tag{63}$$

To satisfy the constraints on $F^{(\zeta),\mathrm{NW}}$ and $F^{(\zeta),\mathrm{SW}}$, we must assign the terms in the first set of brackets on the RHS of (63) to $F^{(\zeta),\mathrm{NW}}$ and those in the second set to $F^{(\zeta),\mathrm{SW}}$. Thus, we now express $F^{(\zeta),\mathrm{NW}}$ and $F^{(\zeta),\mathrm{SW}}$ as follows:

$$F^{(\zeta),\mathrm{NW}}_{i+1/2,j+1/2}=\left[\left\{\overline{F}^{\xi}\left(\frac{1}{2}\bar{q}^{\xi\eta}-\frac{1}{12}(\delta_\eta\bar{q}^{\xi})\right)\right\}_{i,j+1}-\frac{1}{24}G_{i,j+3/2}(\delta_\xi q)_{i,j+1/2}\right]+X_{i+1/2,j+1/2} \tag{64}$$

$$F^{(\zeta),\mathrm{SW}}_{i+1/2,j+1/2}=\left[\left\{\overline{F}^{\xi}\left(\frac{1}{2}\bar{q}^{\xi\eta}+\frac{1}{12}(\delta_\eta\bar{q}^{\xi})\right)\right\}_{i,j}+\frac{1}{24}G_{i,j-1/2}(\delta_\xi q)_{i,j+1/2}\right]-X_{i+1/2,j+1/2} \tag{65}$$

In these, X represents additional terms that $F^{(\zeta),\mathrm{NW}}$ and $F^{(\zeta),\mathrm{SW}}$ may contain that do not appear on the RHS of (49) [because when (64) and (65) are summed, $+X$ in (64) cancels $-X$ in (65)]. There are two constraints which X must satisfy. First, since X appears in both $F^{(\zeta),\mathrm{NW}}$ and $F^{(\zeta),\mathrm{SW}}$, it must satisfy the requirements on the forms of $F^{(\zeta),\mathrm{NW}}$ and $F^{(\zeta),\mathrm{SW}}$ simultaneously. Thus, X must contain mass fluxes and potential vorticities that are evaluated exactly on the line $\eta=\eta_{j+1/2}$ (not above or below it) and on or to the left of the line $\xi=\xi_{i+1/2}$. Second, X must be chosen such that as $\Delta\eta$ goes to zero, $F^{(\zeta),\mathrm{NW}}$ and $F^{(\zeta),\mathrm{SW}}$ each go to zero. This is because the widths (in the $\xi\eta$ plane) of the faces through which $F^{(\zeta),\mathrm{NW}}$ and $F^{(\zeta),\mathrm{SW}}$ pass are each $\Delta\eta/2$ (see Fig. 5), and as these widths are reduced, less and less vorticity can advect through the faces. The most straightforward choice for X that satisfies both these constraints is

$$X_{i+1/2,j+1/2}=\frac{1}{24}G_{i,j+1/2}(\delta_\xi q)_{i,j+1/2} \tag{66}$$

Substituting (66) into (64) and (65), we obtain

$$F^{(\zeta),\mathrm{NW}}_{i+1/2,j+1/2}=\left[\overline{F}^{\xi}\left(\frac{1}{2}\bar{q}^{\xi\eta}-\frac{1}{12}(\delta_\eta\bar{q}^{\xi})\right)\right]_{i,j+1}-\frac{1}{24}(\delta_\eta G)_{i,j+1}(\delta_\xi q)_{i,j+1/2} \tag{67}$$

$$F^{(\zeta),\mathrm{SW}}_{i+1/2,j+1/2}=\left[\overline{F}^{\xi}\left(\frac{1}{2}\bar{q}^{\xi\eta}+\frac{1}{12}(\delta_\eta\bar{q}^{\xi})\right)\right]_{i,j}-\frac{1}{24}(\delta_\eta G)_{i,j}(\delta_\xi q)_{i,j+1/2} \tag{68}$$

This completes our derivation of $F^{(\zeta),\mathrm{NW}}$ and $F^{(\zeta),\mathrm{SW}}$. We can now obtain $F^{(\zeta),\mathrm{NE}}$ and $F^{(\zeta),\mathrm{SE}}$ by substituting (67) and (68) into (57) and (55), respectively, and incrementing the i indices in the resulting expressions by one. We can then use analogous procedures to obtain expressions for the η direction vorticity fluxes $G^{(\zeta),\mathrm{NW}}$, $G^{(\zeta),\mathrm{NE}}$, $G^{(\zeta),\mathrm{SW}}$, and $G^{(\zeta),\mathrm{SE}}$ in (51)–(54). The results are listed in Appendix A.

Next, we derive expressions for the internal vorticity fluxes $\widehat{F}^{(\zeta),\mathrm{N}}$, $\widehat{F}^{(\zeta),\mathrm{S}}$, $\widehat{G}^{(\zeta),\mathrm{E}}$, and $\widehat{G}^{(\zeta),\mathrm{W}}$ (all with i+1/2, j+1/2 subscripts, which we omit for brevity) in terms of nearby mass fluxes and potential vorticities. We first consider $\widehat{F}^{(\zeta),\mathrm{S}}$. Note that this appears both in the vorticity equation for the SW quarter (53) and the one for the SE quarter (54). Following the requirement that the equation for each quarter involve only quantities associated with the h-point CV to which the quarter belongs, we now require that $\widehat{F}^{(\zeta),\mathrm{S}}$ contain mass fluxes and potential vorticities that are evaluated exactly on the line $\xi=\xi_{i+1/2}$ (not to the right or left of it) and on or below the line $\eta=\eta_{j+1/2}$. Also, in order for the overall scheme to conserve domain-summed vorticity, $\widehat{F}^{(\zeta),\mathrm{S}}$ must reduce to zero in the special case in which the face through which it passes is a fluid–land boundary. The simplest expression for $\widehat{F}^{(\zeta),\mathrm{S}}$ that satisfies both these requirements is

$$\widehat{F}^{(\zeta),\mathrm{S}}_{i+1/2,j+1/2}=\frac{1}{2}q_{i+1/2,j+1/2}F_{i+1/2,j} \tag{69}$$

The factor of $1/2$ appears because the face through which $\widehat{F}^{(\zeta),\mathrm{S}}$ passes has width $\Delta\eta/2$ (see Fig. 5). Note that if the h-point at (i,j) or $(i+1,j)$ in Fig. 5 is land, $F_{i+1/2,j}$ will be zero because $(i+1/2,j)$ will be a boundary u-point [see (35)]. As a result, $\widehat{F}^{(\zeta),\mathrm{S}}$ will be zero, as required. Using similar procedures, we can derive the following expressions for the remaining three internal vorticity fluxes:

$$\widehat{F}^{(\zeta),\mathrm{N}}_{i+1/2,j+1/2}=\frac{1}{2}q_{i+1/2,j+1/2}F_{i+1/2,j+1} \tag{70}$$

$$\widehat{G}^{(\zeta),\mathrm{W}}_{i+1/2,j+1/2}=\frac{1}{2}q_{i+1/2,j+1/2}G_{i,j+1/2} \tag{71}$$

$$\widehat{G}^{(\zeta),\mathrm{E}}_{i+1/2,j+1/2}=\frac{1}{2}q_{i+1/2,j+1/2}G_{i+1j+1/2} \tag{72}$$

To complete the derivation of the vorticity equations for the quarters, we must derive expressions for the areas $A^{(\zeta),\mathrm{NW}}$, $A^{(\zeta),\mathrm{NE}}$, $A^{(\zeta),\mathrm{SW}}$, and $A^{(\zeta),\mathrm{SE}}$ associated with each quarter. We can obtain these by forming the vorticity equations for boundary ζ-points at concave corners. Let us first consider such a boundary ζ-point with fluid to the northwest (see Fig. 4a). Since only the northwestern quarter of the full CV centered at this ζ-point is in fluid, the vorticity equation at this ζ-point consists only of the equation for the northwestern quarter. This is given by (51). Since the eastern and southern faces of this quarter are fluid–land boundaries, the mass fluxes $F_{i+1/2,j+1}$ and $G_{i,j+1/2}$ through them are both zero [see (35) and (36)]. As a result, we see from (70) and (71) that the internal vorticity fluxes $\widehat{F}^{(\zeta),\mathrm{N}}$ and $\widehat{G}^{(\zeta),\mathrm{W}}$ appearing in (51) are also zero. Then (51) simplifies to

$$\frac{\mathrm{d}}{\mathrm{d}t}(A^{(\zeta),\mathrm{NW}}\zeta)_{i+1/2,j+1/2} = -[-F^{(\zeta),\mathrm{NW}} + G^{(\zeta),\mathrm{NW}}]_{i+1/2,j+1/2} \tag{73}$$

We will now derive an expression for $A^{(\zeta),\mathrm{NW}}$. This derivation will also yield an expression for the depth $h^{(q)}$ that is needed in calculating q using (20). First, note from (8) that in the continuous case, if at some point in the fluid or at a boundary q does not vary in space, it must also not vary in time, i.e. if $\partial q/\partial\xi = \partial q/\partial\eta = 0$, then $\partial q/\partial t = 0$. We now require that the discrete evolution equation for q corresponding to the discrete vorticity equation (73) also possess this advection property. We can derive the discrete evolution equation for q by setting $\zeta = h^{(q)}q$ in (73) [see (20)]. Doing so and rearranging terms, we get

$$\left(A^{(\zeta),\mathrm{NW}}h^{(q)}\frac{\mathrm{d}q}{\mathrm{d}t}\right)_{i+1/2,j+1/2} = -\left[q\frac{\mathrm{d}}{\mathrm{d}t}(A^{(\zeta),\mathrm{NW}}h^{(q)}) - F^{(\zeta),\mathrm{NW}} + G^{(\zeta),\mathrm{NW}}\right]_{i+1/2,j+1/2}$$

We now set q equal to some spatially uniform value, say $q = q_\mathrm{o}$, and require that $\mathrm{d}q_\mathrm{o}/\mathrm{d}t$ equal zero. This gives (after dividing by q_o)

$$\frac{\mathrm{d}}{\mathrm{d}t}(A^{(\zeta),\mathrm{NW}}h^{(q)})_{i+1/2,j+1/2} = -\frac{1}{4}[(\delta_\xi F)_{i,j+1} + (\delta_\eta G)_{i,j+1}]$$

where we have used (67) and (A.39) with $q = q_\mathrm{o}$ and the fact that $F_{i+1/2,j+1} = G_{i,j+1/2} = 0$ due to the no-flux boundary condition. Using the discrete continuity equation (11) along with the definition of Π given by (12) to substitute for the term in brackets on the RHS, we get

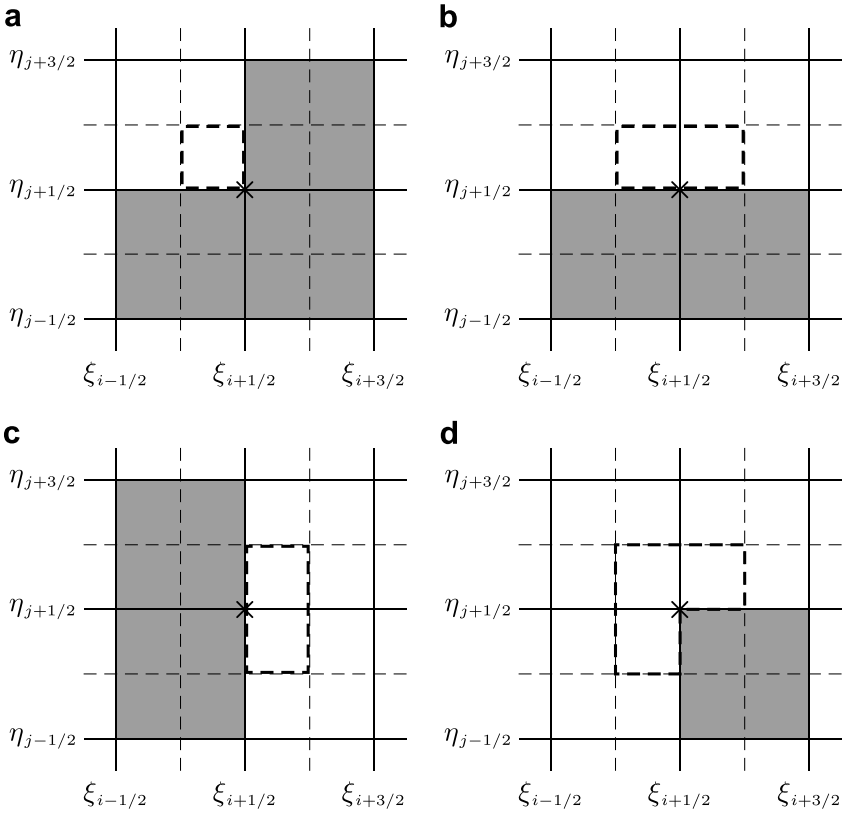

Fig. 4. Example of a fluid–land configuration around a boundary ζ-point in the $\xi\eta$ plane corresponding to a (a) concave corner, (b) horizontal wall, (c) vertical wall, and (d) convex corner. The white h-point CVs are fluid and the shaded ones are land. For each case, the "$\times$" marks the location of the ζ-point, and the thick dashed line segments denote the boundary of the CV associated with the ζ-point.

$$\frac{\mathrm{d}}{\mathrm{d}t}\left(A^{(\zeta),\mathrm{NW}}h^{(q)}\right)_{i+1/2,j+1/2} = \frac{\mathrm{d}}{\mathrm{d}t}\left[\frac{1}{4}A^{(h)}h\right]_{i,j+1} \tag{74}$$

Integrating this with respect to time and solving for $h^{(q)}$, we obtain

$$h^{(q)}_{i+1/2,j+1/2} = \frac{1}{A^{(\zeta),\mathrm{NW}}_{i+1/2,j+1/2}}\left[\frac{1}{4}\left(A^{(h)}h\right)_{i,j+1} + c_{i+1/2,j+1/2}\right] \tag{75}$$

where c is the constant of integration. Since c is independent of time, it cannot be a function of h, u, or v. To obtain an expression for $A^{(\zeta),\mathrm{NW}}$, we now require that when h is spatially uniform, say $h = h_\mathrm{o}$, in the neighborhood of the boundary ζ-point at $(i+1/2, j+1/2)$, (75) give $h^{(q)} = h_\mathrm{o}$. Then, setting $h = h^{(q)} = h_\mathrm{o}$ in (75) and solving for $A^{(\zeta),\mathrm{NW}}$, we obtain

$$A^{(\zeta),\mathrm{NW}}_{i+1/2,j+1/2} = \frac{1}{4}A^{(h)}_{i,j+1} + \frac{1}{h_\mathrm{o}}c_{i+1/2,j+1/2} \tag{76}$$

To determine c, we note that (76) must be valid for all positive values of h_o. Thus, for two distinct values of h_o, say h_1 and h_2, (76) gives

$$A^{(\zeta),\mathrm{NW}}_{i+1/2,j+1/2} = \frac{1}{4}A^{(h)}_{i,j+1} + \frac{1}{h_1}c_{i+1/2,j+1/2} \tag{77}$$

$$A^{(\zeta),\mathrm{NW}}_{i+1/2,j+1/2} = \frac{1}{4}A^{(h)}_{i,j+1} + \frac{1}{h_2}c_{i+1/2,j+1/2} \tag{78}$$

Subtracting (78) from (77) and rearranging terms, we get

$$(h_2 - h_1)c_{i+1/2,j+1/2} = 0$$

Since by assumption h_1 and h_2 are distinct, c must be zero. Then (76)–(78) all reduce to

$$A^{(\zeta),\mathrm{NW}}_{i+1/2,j+1/2} = \frac{1}{4}A^{(h)}_{i,j+1} \tag{79}$$

Substituting (79) into (75) and setting c to zero, we obtain the following expression for $h^{(q)}$:

$$h^{(q)}_{i+1/2,j+1/2} = \frac{\left(A^{(h)}h\right)_{i,j+1}}{A^{(h)}_{i,j+1}} = h_{i,j+1} \tag{80}$$

In terms of Π and $A^{(\zeta),\mathrm{NW}}$, we can rewrite this as

$$h^{(q)}_{i+1/2,j+1/2} = \frac{\Pi_{i,j+1}}{4A^{(\zeta),\mathrm{NW}}_{i+1/2,j+1/2}} \tag{81}$$

To obtain q at the concave corner ζ-point in Fig. 4a, we first solve (73) for ζ using an appropriate time advancement scheme (e.g. the same one used to advance the discrete continuity and momentum equations at fluid h-, u-, and v-points). We then use (80) or (81) to obtain $h^{(q)}$. Finally, we divide ζ by $h^{(q)}$ to obtain q.

We can use similar procedures to derive the vorticity equations and depths $h^{(q)}$ for the remaining 11 boundary ζ-point fluid–land configurations. The procedures for the remaining three concave corners yield expressions for the areas $A^{(\zeta),\mathrm{NE}}$, $A^{(\zeta),\mathrm{SW}}$, and $A^{(\zeta),\mathrm{SE}}$. The results are summarized in Appendix A.

7. Vorticity and potential enstrophy conservation

To prove conservation of domain-summed vorticity, we sum the discrete vorticity equations at fluid ζ-points given by (48) and those at boundary ζ-points given in Appendix A. Recall that by design, the vorticity fluxes out of the faces of a fluid or boundary ζ-point CV match the fluxes into its fluid and/or boundary ζ-point CV neighbors. Also, recall from Section 6 that the vorticity fluxes through boundaries appearing in the boundary vorticity equations are given by the internal vorticity fluxes (69)–(72). Since these are proportional to the mass fluxes, and the mass fluxes through boundaries are zero, the vorticity fluxes through boundaries will also be zero. Thus, when we sum the discrete vorticity equations at fluid and boundary ζ-points, there are no flux contributions from either within the fluid or through the boundaries, and we obtain

$$\frac{\mathrm{d}}{\mathrm{d}t}\left(\mathrm{VORT}_\mathrm{tot}\right) = 0 \tag{82}$$

where the domain-summed vorticity $\mathrm{VORT}_\mathrm{tot}$ is modified from the no-land case given by (29) to include a sum over only fluid and boundary ζ-points, i.e.

$$\mathrm{VORT}_\mathrm{tot} = \sum_{\substack{\text{fld. \& bdy.}\\ \zeta\text{-points}}} \left(A^{(\zeta)}\zeta\right)_{i+1/2,j+1/2} \tag{83}$$

Here, $A^{(\zeta)}$ is the area of a fluid or boundary ζ-point CV. At fluid points, it is given by (25), and at boundary points, it is given by one of the 12 expressions in Appendix A.

We now consider potential enstrophy conservation. Since the AL81 scheme (without land) conserves potential enstrophy, it must be possible to derive a discrete flux-form evolution equation for the potential enstrophy at fluid ζ-points. A detailed derivation of such an equation is given in [36], with the final result given by Eq. (3.161) therein. In that equation, the potential vorticity at fluid ζ-points is defined as

$$r_{i+1/2,j+1/2} = \frac{1}{2}\left(\frac{\zeta^2}{h^{(q)}}\right)_{i+1/2,j+1/2} = \frac{1}{2}(h^{(q)}q^2)_{i+1/2,j+1/2} \tag{84}$$

To derive evolution equations for the potential enstrophy at boundary ζ-points, we first extend the definition (84) to such points. We can then obtain an equation for r at each such point by multiplying the vorticity equation there by q and subtracting from the result the evolution equation for $A^{(\zeta)}h^{(q)}$ multiplied by $q^2/2$. [An evolution equation for $A^{(\zeta)}h^{(q)}$ can be obtained by multiplying the expression for $h^{(q)}$ by $A^{(\zeta)}$, taking $\mathrm{d}/\mathrm{d}t$ of the result, and using the discrete continuity equation (11).] It can be shown (after extensive algebra) that the resulting evolution equations for r at all 12 types of boundary ζ-points listed in Appendix A are in flux form, with the CV for potential enstrophy at a given ζ-point being the same as the one for vorticity at that ζ-point. For example, the potential enstrophy equation at a ζ-point lying on a concave corner with fluid to the northwest (see Fig. 4a) is

$$\frac{\mathrm{d}}{\mathrm{d}t}(A^{(\zeta),\mathrm{NW}}r)_{i+1/2,j+1/2} = -[-F^{(r),\mathrm{NW}} + G^{(r),\mathrm{NW}}]_{i+1/2,j+1/2} \tag{85}$$

where the quantities on the RHS are the potential enstrophy fluxes through the faces of the ζ-point CV in Fig. 4a. Only two fluxes appear because the eastern and southern faces of the CV are no-flux boundaries. These fluxes are given by

$$\begin{aligned} F^{(r),\mathrm{NW}}_{i+1/2,j+1/2} = \overline{F}^{\xi}_{ij+1}&\left[\frac{1}{4}\left\{\overline{q^2}^{\xi} - \frac{1}{2}(\delta_\xi q)^2\right\}_{ij+1/2} - \frac{1}{24}\left\{\overline{(\delta_\eta q)^2}^{\xi} - \frac{1}{2}(\delta_\xi\delta_\eta q)^2\right\}_{ij+1}\right] \\ &+ \left[\frac{1}{24}(\delta_\eta G)_{ij+1}(\delta_\xi q)_{ij+3/2} + \frac{1}{12}G_{ij+1/2}(\delta_\xi\delta_\eta q)_{ij+1}\right]\bar{q}^{\xi}_{ij+1/2} \end{aligned} \tag{86}$$

$$\begin{aligned} G^{(r),\mathrm{NW}}_{i+1/2,j+1/2} = \overline{G}^{\eta}_{ij+1}&\left[\frac{1}{4}\left\{\overline{q^2}^{\eta} - \frac{1}{2}(\delta_\eta q)^2\right\}_{i+1/2,j+1} - \frac{1}{24}\left\{\overline{(\delta_\xi q)^2}^{\eta} - \frac{1}{2}(\delta_\xi\delta_\eta q)^2\right\}_{ij+1}\right] \\ &+ \left[\frac{1}{24}(\delta_\xi F)_{ij+1}(\delta_\eta q)_{i-1/2,j+1} + \frac{1}{12}F_{i+1/2,j+1}(\delta_\xi\delta_\eta q)_{ij+1}\right]\bar{q}^{\eta}_{i+1/2,j+1} \end{aligned} \tag{87}$$

Similar evolution equations can be derived at ζ-points lying on horizontal walls, vertical walls, and convex corners. It can be shown that the potential enstrophy fluxes out of the faces of a fluid or boundary ζ-point CV match the fluxes into its fluid and/or boundary ζ-point CV neighbors. In addition, it can be shown that the potential enstrophy fluxes through those faces of boundary ζ-point CVs that lie on fluid–land boundaries are zero, i.e. they satisfy the no-flux condition. (More specifically, it can be shown that they are proportional to the mass and vorticity fluxes through these fluid–land boundaries, but since the latter two sets of quantities are zero due to the no-flux condition, the potential enstrophy fluxes through fluid–land boundaries will also be zero.) Thus, as with the discrete vorticity equations, when we sum the discrete potential enstrophy equations at fluid and boundary ζ-points, there are no flux contributions from either within the fluid or through the boundaries, and we obtain

$$\frac{\mathrm{d}}{\mathrm{d}t}(\mathrm{PENST}_{\mathrm{tot}}) = 0 \tag{88}$$

where the domain-summed potential enstrophy $\mathrm{PENST}_{\mathrm{tot}}$ is modified from the no-land case given by (30) to include a sum over only fluid and boundary ζ-points, i.e.

$$\mathrm{PENST}_{\mathrm{tot}} = \sum_{\substack{\text{fld. \& bdy.}\\ \zeta\text{-points}}} (A^{(\zeta)}r)_{i+1/2,j+1/2} \tag{89}$$

Eq. (88) proves conservation of $\mathrm{PENST}_{\mathrm{tot}}$. In Section 8.1, we will present numerical simulations demonstrating vorticity and potential enstrophy conservation in the presence of land.

Recall from Section 6 that we derived the discrete evolution equations for the vorticity at boundaries by imposing, among other constraints, vorticity conservation. However, we could instead have imposed potential enstrophy conservation. Had we done so, we would have to solve flux-form evolution equations for the potential enstrophy r instead of for the vorticity ζ at boundary ζ-points. We could have derived evolution equations for r at boundaries using the same strategy we used to obtain the equations for ζ, i.e. by splitting the discrete potential enstrophy equation for AL81 at a fluid ζ-point CV into four – one for each of its quarters – and using as the potential enstrophy equation at a boundary ζ-point the sum of the equations of those quarters that lie in fluid. We have in fact done this and, to our pleasant surprise, found that it yields a set of boundary potential enstrophy equations that is equivalent to the set of boundary vorticity equations listed in Appendix A. This is because if the vorticity evolution equation for a given quarter of a ζ-point CV is used to derive an evolution equation for the

potential enstrophy associated with that quarter, the result is a flux-form equation that is identical to the potential enstrophy equation for that quarter derived by splitting the original AL81 discrete potential enstrophy equation into four parts. Thus, the two approaches (imposing vorticity conservation vs. imposing potential enstrophy conservation) are equivalent. It is for this reason that the scheme we present in this paper converves both vorticity and potential enstrophy. If this were not the case, we would have to choose between vorticity and potential enstrophy conservation, but fortunately we do not have to.

8. Numerical tests

8.1. Conservation

In order to analyze the effect of the boundary scheme on the conservation properties and flow patterns in inviscid SWE models, we now present results from five such models that are identical in all ways except for the way they calculate ζ at boundaries. Away from boundaries, all five models use the AL81 scheme presented in Section 3. Also, all the models use the expressions in Appendix A to calculate $A^{(\zeta)}$ and $h^{(q)}$ at boundary ζ-points, they all use (20) to calculate q at boundary ζ-points, and they all use (38), (46), (83) and (89) to calculate $\mathrm{MASS_{tot}}$, $\mathrm{TE_{tot}}$, $\mathrm{VORT_{tot}}$, and $\mathrm{PENST_{tot}}$ at each discrete time. The five models we will consider are the following:

(1) Boundary vorticity equation model (BVEM)
(2) Extrapolation and finite-differencing model (EFDM)
(3) Free-slip model (FSM)
(4) Super-slip model (SSM)
(5) No-slip model (NSM)

In the BVEM, we use the boundary scheme derived in Section 6 (i.e.we solve evolution equations to obtain ζ at boundaries).In order to time-advance these vorticity equations, we need initial values of ζ at the boundaries.We obtain these using the same method used in the EFDM (described briefly below and in detail in Appendix B).In the remaining four models, we first calculate the relative vorticity ζ_{rel} at boundary ζ-points and then add f to it to obtain the absolute vorticity.In the EFDM, we use extrapolation and finite-differencing on u and v to obtain ζ_{rel} at boundaries.We are interested in this approach because it is the most intuitive alternative to the BVEM. Unlike in the BVEM and EFDM, in the remaining three models we calculate ζ_{rel} at boundaries by enforcing an additional boundary condition (i.e.besides the no-flux condition).In the FSM, we enforce the free-slip condition.This translates to setting ζ_{rel} to zero on boundaries.Recall that this is the method used by Arakawa and Lamb [4], Evans et al.[33], Hart and Evans [34], and Mundt et al.[35] in their periodic channel simulations.In the SSM, we enforce the super-slip condition (see, e.g.[37]).This states that on the boundary, the derivative of ζ_{rel} in the direction normal to the boundary is zero.This boundary condition is most often used in quasigeostrophic models having an explicit dissipation parameterization for ζ_{rel} to set the dissipative flux of ζ_{rel} through the boundaries to zero (see, e.g.[38]).We use it here because it will help illustrate the relationship between the degree of potential enstrophy conservation and the characteristics of the flow field.Finally, in the NSM, we enforce the no-slip condition.This entails setting the velocity tangent to the boundary to zero.Recall that this is the condition used by Mesinger et al.[23] to adapt the scheme of Janjić [9] to domains with arbitrary boundaries.(For more detailed descriptions of the free-slip, super-slip, and no-slip boundary conditions, see, e.g.[37,39,40]).The details of the implementations of the EFDM, FSM, SSM, and NSM are given in AppendixB.

We set up and initialize the simulations as follows. We use Cartesian coordinates $(\xi,\eta)=(x,y)$ and a square domain that extends from -10 to 10 km in both directions. Thus, the dimensions of the domain are $L_x=20$ km by $L_y=20$ km. We assume periodic boundary conditions along the edges of this domain, and we embed in it a rectangular, a triangular, and an elliptic island (Fig. 7). Since bathymetric effects are not the focus of this work, for simplicity we set the bottom topography $h_{\mathrm{bot}}(x,y)$ to zero. Also, in our first set of simulations, we set $f=0$. This allows us to assess the performance of each model in the simplest case of no rotation. We will consider the case of $f\neq 0$ later on. We use a uniform grid with $I\times J=40\times 40$ points, so the grid spacings are $\Delta x=\Delta y=500$ m. We initialize the flow with a rotating core of positive vorticity centered at $(x,y)=(-10\text{ km},0\text{ km})$ given by

$$h(x,y)=50\text{ m} \tag{90}$$

$$u(x,y)=(-2\text{ m s}^{-1})\times\left[\exp\left\{-\left(\frac{x-0.5L_x}{0.1L_x}\right)^2\right\}+\exp\left\{-\left(\frac{x+0.5L_x}{0.1L_x}\right)^2\right\}\right]\times\frac{y}{0.1L_y}\times\exp\left\{-\left(\frac{y}{0.1L_y}\right)^2\right\} \tag{91}$$

$$v(x,y)=(2\text{ m s}^{-1})\times\left[\frac{x-0.5L_x}{0.1L_x}\times\exp\left\{-\left(\frac{x-0.5L_x}{0.1L_x}\right)^2\right\}+\frac{x+0.5L_x}{0.1L_x}\times\exp\left\{-\left(\frac{x+0.5L_x}{0.1L_x}\right)^2\right\}\right]\times\exp\left\{-\left(\frac{y}{0.1L_y}\right)^2\right\} \tag{92}$$

The initial velocity and vorticity fields are shown in Fig. 7a.

To advect the initial vorticity core toward and around the islands, we gradually force a westerly flow by adding the source term $S_\xi/(mh) = S_x/h$ to the RHS of the $\xi = x$ direction momentum equation (2). Here, S_x is a stress term given by

$$S_x = (3.5 \times 10^{-3}\ \mathrm{m^2\ s^{-2}}) \times \frac{h}{50\ \mathrm{m}} \times \frac{1}{2}\left[\mathrm{erf}\left(\frac{t-t_1}{t_0}\right) - \mathrm{erf}\left(\frac{t-t_2}{t_0}\right)\right] \tag{93}$$

where erf(...) is the error function and $t_0 = 1000$ s, $t_1 = 5000$ s, and $t_2 = 10{,}000$ s. (93) corresponds to an input of westerly momentum between $t \approx t_1$ and $t \approx t_2$. There is no source term on the RHS of the $\eta = y$ direction momentum equation (3), i.e. $S_\eta/(nh) = S_y/h = 0$. The corresponding source term on the right-hand side of the flux-form vorticity equation (7) is

$$\frac{\partial}{\partial \xi}\left(\frac{S_\eta}{nh}\right) - \frac{\partial}{\partial \eta}\left(\frac{S_\xi}{mh}\right) = 0 - \frac{\partial}{\partial y}\left(\frac{S_x}{h}\right) = 0 \tag{94}$$

The right-hand side of (94) is zero because S_x/h is spatially uniform. Thus, (93) does not generate any new vorticity or potential enstrophy. It of course generates energy, but this is limited to $t_1 \lesssim t \lesssim t_2$. Thus, an energy conserving model will maintain a constant $\mathrm{TE_{tot}}$ for $t \gtrsim t_2$.

We integrate all five models to $t = 10^6$ s ≈ 11.6 d using the fourth-order Runge–Kutta (RK4) method and a time step of $\Delta t = 20$ s. Since all the models use the flux-form discrete continuity equation (11), they all conserve $\mathrm{MASS_{tot}}$. To determine whether they also conserve $\mathrm{TE_{tot}}$, $\mathrm{VORT_{tot}}$, and $\mathrm{PENST_{tot}}$, we plot the deviations of these quantities from their initial values as functions of time. These deviations are defined by

$$\Delta \mathrm{TE_{tot}} = \mathrm{TE_{tot}} - \mathrm{TE_{tot,init}} \tag{95}$$

$$\Delta \mathrm{VORT_{tot}} = \mathrm{VORT_{tot}} - \mathrm{VORT_{tot,init}} \tag{96}$$

$$\Delta \mathrm{PENST_{tot}} = \mathrm{PENST_{tot}} - \mathrm{PENST_{tot,init}} \tag{97}$$

where the "init" subscripts denote initial values.

Fig. 6 shows the evolution of $\Delta \mathrm{TE_{tot}}$, $\Delta \mathrm{VORT_{tot}}$, and $\Delta \mathrm{PENST_{tot}}$ for each of the five models. For clarity, we have split the $\Delta \mathrm{VORT_{tot}}$ curves between Figs. 6c and d, and we have plotted the absolute value of $\Delta \mathrm{PENST_{tot}}$ on a log scale in Fig. 6b. We can see from Fig. 6a that the curves for $\Delta \mathrm{TE_{tot}}$ are virtually identical. As expected, they increase between t_1 and t_2 due to

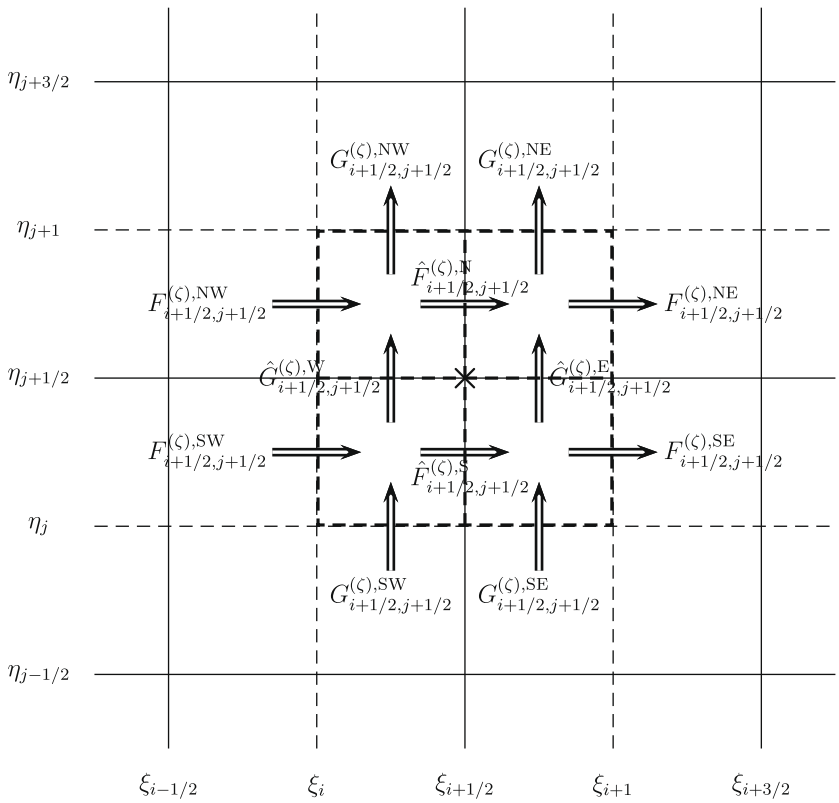

Fig. 5. The quarters comprising a fluid ζ-point CV in the $\xi\eta$ plane and the vorticity fluxes through their faces. The thick dashed line segments denote the boundaries of the quarters, and the arrows denote the vorticity fluxes. The "×" marks the location of the ζ-point.

the momentum source and remain constant afterward. This indicates that all five models conserve TE_{tot}, as anticipated from the analysis in Section 5. It is also clear from Figs. 6c and d that the BVEM conserves $VORT_{tot}$ [as expected from (82)] but the other models do not. The variations in $\Delta VORT_{tot}$ in the BVEM are on the order of 10^{-11} m^2 s^{-1} (which are too small to see in the plot) while those in the other four models are on the order of 1000 m^2 s^{-1}. Finally, we can see from Fig. 6b that the BVEM and FSM conserve $PENST_{tot}$ to a far greater extent than the other three models. For the BVEM and FSM, the maximum values of $|\Delta PENST_{tot}|$ over the course of the simulation are 1.63×10^{-9} m s^{-2} and 1.46×10^{-9} m s^{-2}. The corresponding values for the EFDM, SSM, and NSM are 5.81, 0.577, and 6.80 m s^{-2}. We have performed a refinement study on the time step Δt (not shown) and have found that $\Delta PENST_{tot}$ in the BVEM and FSM goes to zero as Δt is reduced. This indicates that in these two models, the time integration is the only source of error in $PENST_{tot}$; the boundary treatment is not a source or sink of potential enstrophy. For the BVEM, this behavior is in agreement with the potential enstrophy conservation result (88). It can be shown analytically that (88) also holds for the FSM when $f = 0$. This is merely a fortunate coincidence; it is not by design. Nevertheless, it explains why variations in $\Delta PENST_{tot}$ in the FSM are due to only time integration errors. On the other hand, in the EFDM, SSM, and NSM, $\Delta PENST_{tot}$ does not go to zero as Δt is reduced. Thus, variations in $\Delta PENST_{tot}$ in these models must be due to spurious sources and sinks of potential enstrophy at the boundaries.

To relate the conservation characteristics of the five models to the flow fields generated by each, we show in Figs. 7b–f the velocity and vorticity fields at $t = 10^6$ s. For ease of comparison, we use the same vector length scale for the velocity and the same gray scale for the vorticity in all the figures. Note that the velocity fields in these figures are comparable in magnitude; typical velocities in all five cases are on the order of 1 m s^{-1}. This is because all the models conserve TE_{tot}, and this keeps the velocities bounded. However, bounded velocities do not necessarily translate to well-behaved energy spectra. A close examination of the velocity fields in Fig. 7 reveals that in the BVEM and FSM, most of the kinetic energy remains in the large scales while in the EFDM and NSM, most of it is in the small scales. The SSM falls somewhere in between. This correlates well with the extent to which each model conserves $PENST_{tot}$. The BVEM and FSM conserve $PENST_{tot}$ almost exactly (with any errors due to only the time integration) while the EFDM and NSM do not conserve $PENST_{tot}$. The SSM also does not conserve $PENST_{tot}$, but it does a better job than the EFDM and NSM by about an order of magnitude (see Fig. 6b). The $PENST_{tot}$ conservation characteristics of the models are also reflected in the vorticity fields they generate. We can see in Fig. 7 that the fields generated by the EFDM and NSM are noisier and have larger magnitudes (by a factor of about 5–10) than the ones generated by the BVEM and FSM. As above, the SSM falls somewhere in between. This is because in the BVEM and FSM, $PENST_{tot}$ conservation keeps the vorticity magnitude at each ζ-point bounded, but in the EFDM, SSM, and NSM, there is no such constraint.

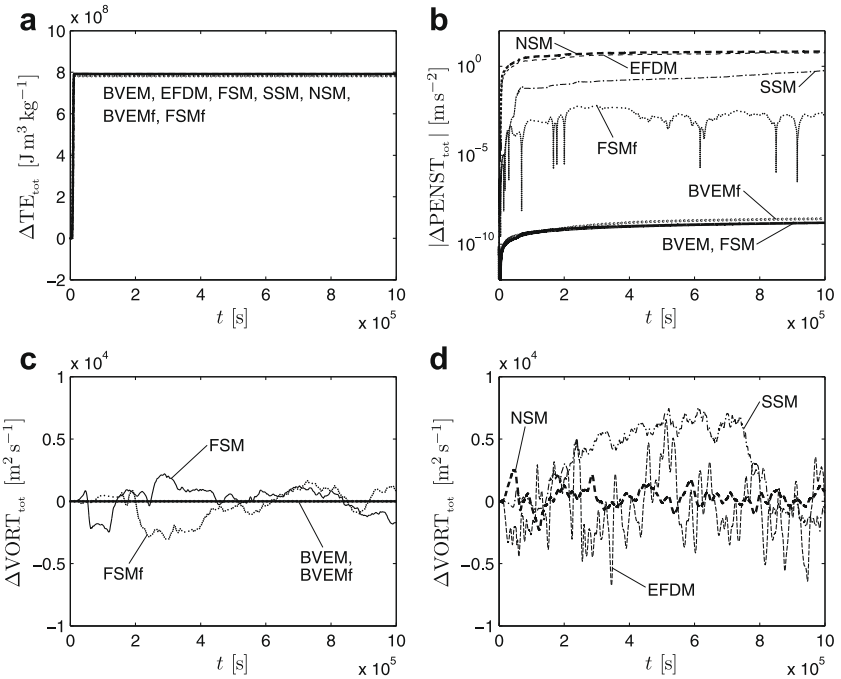

Fig. 6. Plots of the deviations from initial values of the domain-summed energy ΔTE_{tot}, vorticity $\Delta VORT_{tot}$, and potential enstrophy $\Delta PENST_{tot}$ as functions of time for the simulations using the five models discussed in Section 8.1. (a) Shows ΔTE_{tot} for all five models. The jump in ΔTE_{tot} shortly after $t = 0$ (which is present in all the models) is due to the input of energy by the momentum source term S_x given by (93). (b) shows the absolute value of $\Delta PENST_{tot}$ for all five models. Note that the vertical axis uses logarithmic scaling. (c) shows $\Delta VORT_{tot}$ for the BVEM, FSM, BVEMf, and FSMf, and (d) shows $\Delta VORT_{tot}$ for the SSM, EFDM, and NSM. We use thick solid lines for the BVEM, thin dashed lines for the EFDM, thin solid lines for the FSM, dot-dashed lines for the SSM, thick dashed lines for the NSM, thick dotted lines for the BVEMf, and thin dotted lines for the FSMf.

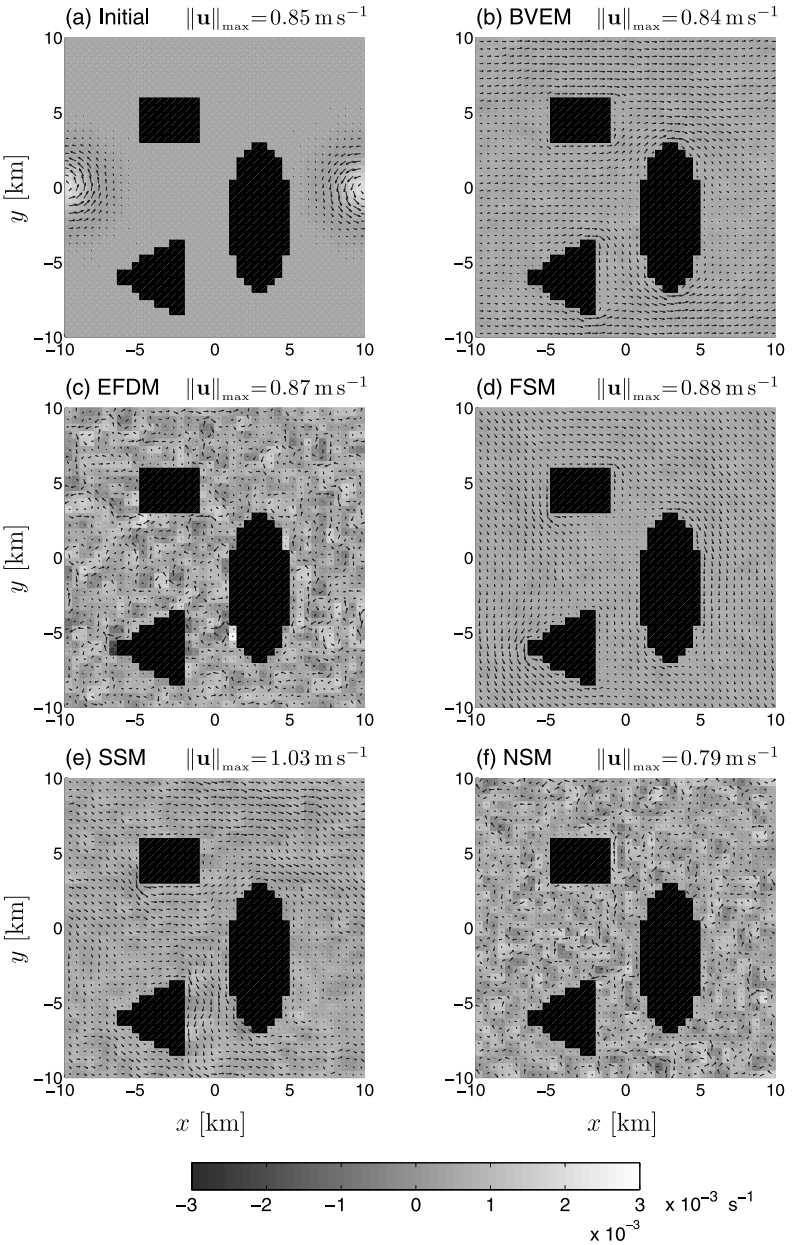

Fig. 7. Velocity vectors and vorticity field at (a) $t = 0$ s and at $t = 10^6$ s ≈ 11.6 d for the (b) BVEM, (c) EFDM, (d) FSM, (e) SSM, and (f) NSM simulations. The black regions are land. All six plots use the same vector length scale for the velocity and the same gray scale for the vorticity. All five simulations are without rotation ($f = 0$). The maximum velocity magnitude $\|\boldsymbol{u}\|_{\max}$ for each plot is given in the plot title. For plotting purposes, u, v, and ζ have been averaged from u-, v-, and ζ-points, respectively, to h-points. The BVEM and FSM produce the least small-scale noise, but the BVEM is the only model that maintains a generally westerly flow that is consistent with the westerly direction of the forcing.

Recall that all five models considered here use the mass, energy, vorticity, and potential enstrophy conserving AL81 scheme away from fluid–land boundaries. Thus, our results indicate that in order to prevent a spurious energy cascade to the smallest resolved scales, it is not sufficient to use such a scheme only within the fluid; the boundaries must also be treated in such a way that $\mathrm{PENST_{tot}}$ is conserved. Otherwise, errors generated at the boundaries can contaminate the rest of the flow. The extent of this contamination seems to depend on the extent of non-conservation of $\mathrm{PENST_{tot}}$. Since out of the five models analyzed the BVEM and FSM are the only two that conserve $\mathrm{PENST_{tot}}$, we will henceforth consider only these two models.

Recall that the BVEM and FSM both conserve $\mathrm{MASS_{tot}}$, $\mathrm{TE_{tot}}$, and $\mathrm{PENST_{tot}}$, but only the BVEM also conserves $\mathrm{VORT_{tot}}$. To determine if this difference in conservation properties translates into a difference in flow pattern between the two models,

we compare the velocity fields in Figs. 7b and d. We can see from Fig. 7b that the velocity field generated by the BVEM is generally westerly. This agrees well with the direction of the forcing, which is purely westerly [see (93)]. Thus, the BVEM redistributes the vorticity in the initial rotating core in such a way that the large-scale flow remains oriented in the direction of the forcing. On the other hand, we can see from Fig. 7d that the velocity field generated by the FSM is for the most part southerly or southeasterly. The difference in the overall flow orientation between the two models must be due to the spurious sources and sinks of vorticity in the FSM (which cause it to violate $\mathrm{VORT}_{\mathrm{tot}}$ conservation). These inject vorticity into the flow at the boundaries. This new vorticity is then redistributed throughout the domain, and its overall effect is to turn the large-scale flow away from the direction of the forcing.

Finally, we demonstrate that only the BVEM conserves $\mathrm{PENST}_{\mathrm{tot}}$ when rotation is included. We do this by rerunning the BVEM and FSM simulations above with $f = 10^{-4}\ \mathrm{s}^{-1}$. We denote these simulations by BVEMf and FSMf, respectively. Fig. 6 shows the evolution of $\Delta\mathrm{TE}_{\mathrm{tot}},\ \Delta\mathrm{VORT}_{\mathrm{tot}}$, and $\Delta\mathrm{PENST}_{\mathrm{tot}}$ for these two simulations. We can see in Fig. 6a that both of these simulations conserve $\mathrm{TE}_{\mathrm{tot}}$, and we can see in Fig. 6c that the BVEMf conserves $\mathrm{VORT}_{\mathrm{tot}}$ while the FSMf does not. Also, we can see in Fig. 6b that the $|\Delta\mathrm{PENST}_{\mathrm{tot}}|$ curve for the BVEMf is very close to the curve for the BVEM, indicating that the variations in $\Delta\mathrm{PENST}_{\mathrm{tot}}$ in the BVEMf are due only to truncation errors in the time integration. On the other hand, the $|\Delta\mathrm{PENST}_{\mathrm{tot}}|$ curve for the FSMf is much higher than the curve for the FSM. The maximum value of $|\Delta\mathrm{PENST}_{\mathrm{tot}}|$ over the course of the FSMf simulation is $6.16 \times 10^{-3}\ \mathrm{m\ s}^{-2}$. Recall that the corresponding value for the FSM is $1.46 \times 10^{-9}\ \mathrm{m\ s}^{-2}$. Thus, $\mathrm{PENST}_{\mathrm{tot}}$ is not conserved in the FSMf simulation.

We note here that, as pointed out by Hollingsworth et al. [41], the AL81 scheme does not conserve momentum. As a result, when applied to the 3D hydrostatic equations, it generates an internal instability. Hollingsworth et al. [41] present a modification to their EE scheme (which also suffers from this instability) that eliminates the instability while maintaining the mass, energy, vorticity, and enstrophy (but not potential enstrophy) conserving properties of the scheme. The instability is eliminated because the modified EE scheme conserves momentum for the linearized SWEs. If this shortcoming of AL81 is a concern, it is likely that an approach similar to the one presented in this paper can be used to derive a boundary scheme for the modified EE scheme. We suspect this because the AL81 and modified EE schemes both discretize the rotational form of the SWEs on the C-grid. However, we have not attempted it.

8.2. Accuracy

Maintaining global conservation properties is necessary in long-term global-scale climate and ocean simulations in order to keep such simulations stable and to obtain statistically unbiased results [3]. Thus, the conservative boundary scheme presented in this paper (the BVEM) is well-suited for such simulations. However, we also intend to use the BVEM for short-term regional simulations. In such simulations, numerical accuracy is of primary importance because the goal is to obtain as accurate a forecast as possible; conservation properties are of secondary importance because the simulation times are not long enough for biases due to non-conservation to develop (although Tripoli [8] has found that imposing energy and enstrophy conservation is beneficial even in short-term atmospheric simulations). Thus, we will now analyze the spatial accuracy of the BVEM and compare it with those of the four other models considered in Section 8.1.

We will determine the accuracy of a given model by performing grid refinement studies (GRSs). This entails simulating the same flow configuration on a set of successively finer grids, calculating various norms of the errors in the dependent variables $h,\ u_\xi,\ u_\eta$, and ζ, and observing their behaviors as the grid spacing is reduced (i.e. their magnitudes and rates of convergence to zero). (We have reverted back to using subscripts on the velocity components because below, we will need to distinguish between the Cartesian components u and v and the cylindrical components u_r and u_θ.) We consider the following three geometric/coordinate system configurations:

(1) Axisymmetric flow in an annulus in cylindrical coordinates (ANU_cyln)
(2) Axisymmetric flow in an annulus in Cartesian coordinates (ANU_Cart)
(3) Advection of a core of vorticity around an elliptic island in Cartesian coordinates (VCOR_ISL)

We perform the GRSs of ANU_cyln and ANU_Cart with all five models, but we perform only one GRS of VCOR_ISL using the BVEM. The error norms we calculate are the standard $L_1,\ L_2$, and L_∞ norms and modified forms of these which we refer to as the $L_1',\ L_2'$, and L_∞' norms. The definitions of these norms and the methods used to calculate them are given in Appendix D. The only difference between these two sets of norms is that the former span the whole flow domain while the latter exclude one layer of h-point CVs adjacent to boundaries on the coarsest grid. For the GRSs of ANU_cyln and ANU_Cart, we calculate the errors in both sets of norms. This is useful because any differences between the two sets reveals the behavior of the error at and/or near the boundaries. For the GRS of VCOR_ISL, we only calculate the $L_1',\ L_2'$, and L_∞' error norms; we cannot calculate the $L_1,\ L_2$, and L_∞ norms due to difficulties in obtaining (approximations to) the exact solution at h-point CVs adjacent to boundaries. This issue is discussed in detail in Appendix D.

The motivation for simulating axisymmetric flow in an annulus in both cylindrical and Cartesian coordinates is to evaluate the significance of geometric errors (i.e. errors that arise because the location of the boundary must be approximated on the grid by stair-steps). In cylindrical coordinates $(\xi, \eta) = (r, \theta)$, we can completely eliminate geometric errors by placing one vertical grid line (vertical as seen in the $r\theta$ plane) exactly on the inner boundary of the annulus and another exactly on its outer boundary and taking these two grid lines to be the model boundaries. We can do this because, like the annulus

boundaries, these vertical grid lines are lines of constant r. Note also that in cylindrical coordinates, the locations of the model boundaries do not change as we move from coarser to finer grids. On the other hand, there are geometric errors in Cartesian coordinates $(\xi,\eta)=(x,y)$ because the circular boundaries of the annulus must be approximated by stair-steps. In addition, as we move from coarser to finer grids, the locations of the model boundaries change in order to better approximate the shapes of the exact boundaries (although this change becomes smaller and smaller as we move to finer grids). Thus, any differences in the behaviors of the errors between the GRSs of ANU_cyln and the GRSs of ANU_Cart will be due to the presence of geometric errors in the latter. (To be more precise, we should also consider errors due to the time integration. However, like Salmon [22], we have found that these are always much smaller than geometric and spatial truncation errors; the results of our GRSs are not affected by the choice of time step Δt as long as we choose a Δt for which the integration is stable. Thus, we can safely ignore the time integration errors.)

The annulus geometry, initial conditions, and forcing we will use in the GRSs of ANU_cyln and ANU_Cart are as follows. The inner boundary of the annulus is at $r=5$ km, and the outer boundary is at $r=25$ km. Initially, the fluid is at rest and has a uniform depth of 5 m. In cylindrical coordinates, we initiate motion in the azimuthal direction using the source term $S_\eta/(nh)=rS_\theta/h$ on the RHS of the $\eta=\theta$ direction momentum equation (3). Here, S_θ is a stress term given by

$$S_\theta=(10^{-3}\ \mathrm{m^2\ s^{-2}})\times\frac{h}{5\ \mathrm{m}}\times\sin\left(\frac{1.4\pi}{20\ \mathrm{km}}r\right)\times\frac{1}{2}\left[\mathrm{erf}\left(\frac{t-t_1}{t_0}\right)-\mathrm{erf}\left(\frac{t-t_2}{t_0}\right)\right] \tag{98}$$

where $t_0,\ t_1$, and t_2 in (98) have the same values as in (93). S_θ provides a gradual input of azimuthal momentum between $t\approx t_1=5000$ s and $t\approx t_2=10{,}000$ s. It generates vorticity as a function of r throughout the domain, including at the boundaries. Thus, it will test the ability of each model to advect vorticity along the boundaries. There is no source term on the RHS of the $\xi=r$ direction momentum equation (2), i.e. $S_\xi/(mh)=S_r/h=0$. The corresponding source term on the RHS of the flux-form vorticity equation (7) is

$$\frac{\partial}{\partial\xi}\left(\frac{S_\eta}{nh}\right)-\frac{\partial}{\partial\eta}\left(\frac{S_\xi}{mh}\right)=\frac{\partial}{\partial r}\left(\frac{rS_\theta}{h}\right)-\frac{\partial}{\partial\theta}\left(\frac{S_r}{h}\right)=\frac{\partial}{\partial r}\left(\frac{rS_\theta}{h}\right) \tag{99}$$

In Cartesian coordinates, we initiate motion using the forcing functions $S_\xi/(mh)=S_x/h$ and $S_\eta/(nh)=S_y/h$ on the RHSs of the x and y direction momentum equations (2) and (3). The Cartesian stress components S_x and S_y are obtained using a vector component transformation from cylindrical to Cartesian coordinates, i.e.

$$S_x=S_r\cos\theta-S_\theta\sin\theta=-S_\theta\sin\theta=-\frac{y}{r}S_\theta(r) \tag{100}$$

$$S_y=S_r\sin\theta+S_\theta\cos\theta=S_\theta\cos\theta=\frac{x}{r}S_\theta(r) \tag{101}$$

where $r=(x^2+y^2)^{1/2}$. The corresponding source term on the RHS of the flux-form vorticity equation (7) is

$$\frac{\partial}{\partial\xi}\left(\frac{S_\eta}{nh}\right)-\frac{\partial}{\partial\eta}\left(\frac{S_\xi}{mh}\right)=\frac{\partial}{\partial x}\left(\frac{S_y}{h}\right)-\frac{\partial}{\partial y}\left(\frac{S_x}{h}\right) \tag{102}$$

In the BVEM, we include a discrete counterpart of (99) or (102) (properly weighted by the areas of the boundary ζ-point CVs) on the RHS of the vorticity equation at each boundary ζ-point. To calculate the derivative(s) in this discrete counterpart, we first fit a quadratic polynomial of $r,\ x$, or y to $rS_\theta/h,\ S_y/h$, or S_x/h using values of these quantities at the boundary ζ-point and the two nearest u- or v-points. We then take the derivative of the polynomial and evaluate it at the boundary ζ-point. We integrate all simulations to $t=10^5$ s ≈ 1.16 d using RK4. The time steps used are specified below. Also, for simplicity, we set $f=0$ in all simulations discussed in this section.

We set up the model grids in the GRSs of ANU_cyln and ANU_Cart as follows. In the GRSs of ANU_cyln, we locate the computational grid in the $r\theta$ plane such that one vertical grid line coincides with the boundary at $r=5$ km and another with the boundary at $r=25$ km, and we take these two grid lines to be the model boundaries. Since the flow is axisymmetric, the solution will not be a function of θ. Thus, we use only one grid point in θ and assume periodic boundary conditions in the θ direction (in agreement with the axisymmetric nature of the flow). We use the following successive numbers of grid points in r: 40, 80, 160, 320, 640, 1280, 2560, 5120, and 10,240. The corresponding time steps are 20, 20, 10, 5, 4, 2, 1, 0.5, and 0.25 s. The radial grid size Δr is 500 m on the coarsest grid and 1.953125 m on the finest. In the GRSs of ANU_Cart, we reduce memory usage and computation time by simulating the flow in only the upper-right quarter of the annulus in the xy plane, assuming that any fluid that exits through the upper-left side of this quarter reenters through its lower-right side and vice versa. We can do this because the flow is axisymmetric; thus, each of the four quarters will have the same solution (to within a geometric rotation). We use grids with the following numbers of grid points in x and y to resolve the upper-right quarter: $52\times52,\ 104\times104,\ 208\times208,\ 416\times416$, and 832×832. The corresponding time steps are 20, 20, 10, 5, and 4 s. The grid size is $\Delta x=\Delta y=500$ m on the coarsest grid and 31.25 m on the finest. We do not use grids any finer than 832×832 because the memory requirements and computation times become prohibitive.

The original AL81 scheme (without land) is second-order accurate in $\Delta\xi$ and $\Delta\eta$. Thus, the best we can expect from the five boundary models is second-order convergence of the errors. We have plotted the $L_1,\ L_2$, and L_∞ as well as the $L_1',\ L_2'$, and L_∞' error norms of h, the velocity components u_r and u_θ or u and v, and ζ as functions of the grid spacing at every 500 s. Note that for both the GRSs of ANU_cyln and the GRSs of ANU_Cart, we use the 10,240-point simulation in cylindrical coordinates

with the BVEM as the "exact" solution in order to calculate the error norms. This issue is discussed in Appendix D. Table 1 lists the rates of convergence to zero of the error norms for all five models for both the GRSs of ANU_cyln and the GRSs of ANU_Cart. In the GRSs of ANU_cyln, the error norms as functions of Δr are almost exactly linear (on a log–log plot). In addition, the convergence rates stay essentially unchanged for all four dependent variables from about the beginning of the forcing at $t \approx 5000$ s to the final time of $t = 10^5$ s. In the GRSs of ANU_Cart, the error norms for the BVEM, FSM, and SSM are either also very linear functions of Δx or Δy or are only slightly irregular (i.e. jagged). For the slightly irregular cases, we specify a range for the convergence rate in Table 1. For the BVEM, FSM, and SSM, the convergence rates of the error norms of $h,\ u$, and v stay essentially unchanged from $t \approx 5000$ s to $t = 10^5$ s while the rates for ζ remain mostly unchanged after the end of the forcing at $t \approx 10{,}000$ s to $t = 10^5$ s. On the other hand, the error norms for the EFDM and NSM in the GRSs of ANU_Cart are usually very irregular functions of Δx or Δy, and they vary significantly in time. In these cases, it is difficult to determine even a range for the convergence rate. Thus, in Table 1, we label these cases "irreg." (irregular).

The results of the GRSs of ANU_cyln – both in terms of the magnitudes of the error norms and their convergence rates – can be summarized as follows. The NSM has the lowest overall accuracy, followed by the FSM, followed in order of increasing accuracy by the SSM, BVEM, and EFDM. The differences between the last three are small, found only in the magnitudes and convergence rates of $\|\Delta\zeta\|_1,\ \|\Delta\zeta\|_2$, and $\|\Delta\zeta\|_\infty$ (i.e. the $L_1,\ L_2$, and L_∞ error norms of ζ). As an example, we show in Fig. 8 plots of $\|\Delta\zeta\|_1,\ \|\Delta\zeta\|_2$, and $\|\Delta\zeta\|_\infty$ vs. Δr at $t = 10^5$ s. For reference, we include all five models in the plots. Recall that these plots are representative of the error norms of ζ throughout most of the integration period. A comparison of the SSM, BVEM, and EFDM error norms in Fig. 8 shows that the SSM has the largest values for all three error norms. In addition, it has the same convergence rate as the BVEM and EFDM for $\|\Delta\zeta\|_1$ (a rate of 2) but has lower convergence rates for $\|\Delta\zeta\|_2$ and $\|\Delta\zeta\|_\infty$ (1.5 and 1 for the SSM vs. 2 and 1.1 for the BVEM and 2 and 2 for the EFDM). The BVEM and EFDM have almost identical magnitudes and rates of convergence for $\|\Delta\zeta\|_1$ and $\|\Delta\zeta\|_2$, but the EFDM has a higher convergence rate for $\|\Delta\zeta\|_\infty$ (2 vs. 1.1 for the BVEM).

Next, we consider the GRSs of ANU_Cart. Although the EFDM does very well in the cylindrical case, it breaks down completely in the Cartesian case. We can see this by the fact that none of its error norms in Table 1 converge; in fact, the ones of ζ all diverge. This failure can be traced back to the calculation of the vorticity at convex corners using finite-differencing. The NSM also performs quite poorly in Cartesian coordinates. For both these models, we observe grid-scale oscillations in $h,\ u,\ v$, and ζ throughout the domain. For this reason, we consider these boundary models unfit for solving the inviscid SWEs in the general case in which the exact boundaries are not aligned with the model grid lines (and thus must be approximated by stair-steps). The remaining three models – the BVEM, FSM, and SSM – have almost identical magnitudes and rates of convergence for the six error norms of $h,\ u$, and v. However, differences between these three models exist in the error norms of ζ. As an example, we show in Fig. 9 plots of $\|\Delta\zeta\|_1,\ \|\Delta\zeta\|_2$, and $\|\Delta\zeta\|_\infty$ vs. Δx or Δy at $t = 10^5$ s. For comparison with Fig. 8, we include all five models in these plots. From the figure, we can see that the FSM has larger error magnitudes and smaller convergence rates than the BVEM and SSM. This is the case throughout the integration. Thus, the FSM does not perform as well as the BVEM or SSM with respect to these three error norms of ζ. We can also see from Fig. 9 that $\|\Delta\zeta\|_1,\ \|\Delta\zeta\|_2$, and $\|\Delta\zeta\|_\infty$ for the SSM are always larger than for the BVEM (and again, this is the case throughout the integration). These differences are small for $\|\Delta\zeta\|_1$ and $\|\Delta\zeta\|_2$ but can be significant for $\|\Delta\zeta\|_\infty$. For example, at a resolution of

Table 1
Rates of convergence of the various error norms of h, the velocity components, and ζ with decreasing grid size for the five models used in the grid resolution studies of axisymmetric flow in an annulus in cylindrical (ANU_cyln) and Cartesian (ANU_Cart) coordinates

		Cylindrical (ANU_cyln)								Cartesian (ANU_Cart)							
		h		u_r		u_θ		ζ		h		u		v		ζ	
		L[a]	L'	L	L'	L	L'	L	L'	L	L'	L	L'	L	L'	L	L'
BVEM	1	2	2	2	2	2	2	2	2	1	1–1.25	1	1–1.25	1	1–1.25	1–1.25	1–1.25
	2	2	2	2	2	2	2	2	2	0.5	1–1.25	0.5	1–1.25	0.5	1–1.25	1–1.25	1–1.25
	∞	2	2	2	2	2	2	1.1	2	0	1–1.25	0	1.5	0	1.5	0.75–1	1–1.25
EFDM	1	2	2	2	2	2	2	2	2	irreg.[b]	irreg.	irreg.	irreg.	irreg.	irreg.	div.[c]	div.
	2	2	2	2	2	2	2	2	2	irreg.	irreg.	irreg.	irreg.	irreg.	irreg.	div.	div.
	∞	2	2	2	2	2	2	2	2	irreg.	irreg.	irreg.	irreg.	irreg.	irreg.	div.	div.
FSM	1	2	2	2	2	2	2	1	2	1	1–1.25	1	1–1.25	1	1–1.25	0.75	0.5–0.75
	2	1.5	2	2	2	2	2	0.5	2	0.5	1–1.25	0.5	1–1.25	0.5	1–1.25	0.5	0.5–0.75
	∞	1	2	2	2	1	2	0	2	0	1–1.25	0	1.5	0	1.5	0	irreg.
SSM	1	2	2	2	2	2	2	2	2	1	1–1.25	1	1–1.25	1	1–1.25	1–1.25	1–1.25
	2	2	2	2	2	2	2	1.5	2	0.5	1–1.25	0.5	1–1.25	0.5	1–1.25	1.25	1–1.25
	∞	2	2	2	2	2	2	1	2	0	1–1.25	0	1.5	0	1.5	1–1.25	0.75–1.25
NSM	1	1	1	1	1	1	1	0	1	0.25–0.5	0.25–0.5	0–0.5	0–0.5	0–0.5	0–0.5	div.	div.
	2	0.5	1	1	1	0.5	1	div.	1	0.5–0.75	0.25–0.75	0–0.5	0–0.5	0–0.5	0–0.5	div.	div.
	∞	0	1	1	1	0	1	div.	1	irreg.	irreg.	irreg.	irreg.	irreg.	irreg.	div.	div.

[a] $L_1,\ L_2$, and L_∞ are the norms with all fluid h-points in the domain included, and $L'_1,\ L'_2$, and L'_∞ are the norms with the layer of coarsest-grid h-points adjacent to the boundary excluded (see Appendix D).

[b] "irreg." indicates an irregular (i.e. jagged) dependence of the error norm on the grid size. In such cases, it is difficult to determine a rate of convergence.

[c] "div." indicates that the error norm grows (diverges) with decreasing grid size.

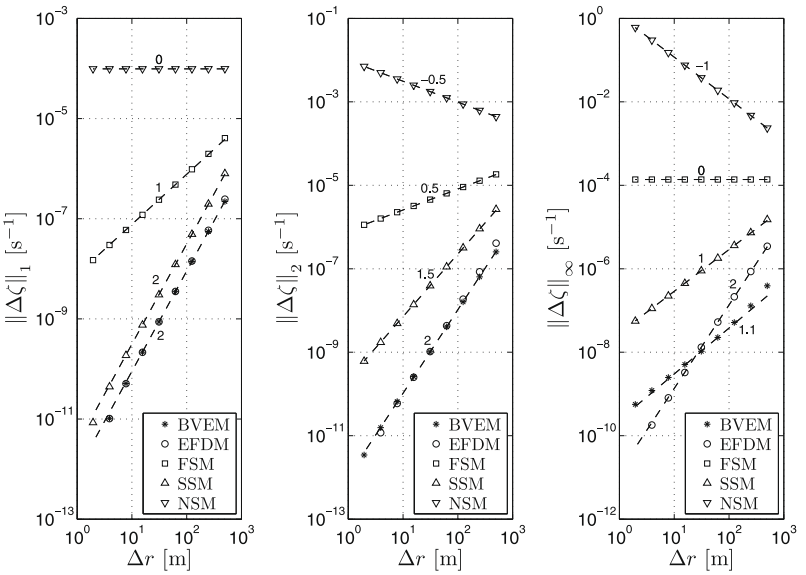

Fig. 8. L_1, L_2, and L_∞ error norms of ζ at $t = 10^5$ s from the grid refinement studies of axisymmetric flow in an annulus in cylindrical coordinates (ANU_cyln). Results from all five boundary models are shown. The dashed lines are reference lines having the indicated slopes. The solution from the 10,240-point simulation with the EFDM is taken as the "exact" solution in order to calculate the errors in all five models (see Appendix D). For this reason, there are nine data points for the BVEM, FSM, SSM, and NSM corresponding to the nine grids but only eight for the EFDM (the ninth point has a value of zero). The data point for $\|\Delta\zeta\|_1$ for the BVEM on the finest grid ($\Delta r = 1.953125$ m) does not appear because its value is less than 10^{-13} s^{-1}.

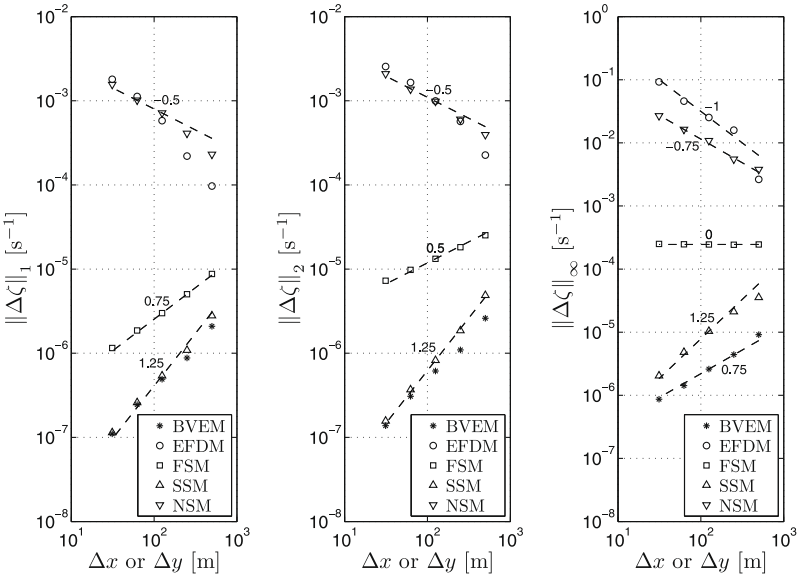

Fig. 9. L_1, L_2, and L_∞ error norms of ζ at $t = 10^5$ s from the grid refinement studies of axisymmetric flow in an annulus in Cartesian coordinates (ANU_Cart). Results from all five boundary models are shown. The dashed lines are reference lines having the indicated slopes. The solution from the 10,240-point cylindrical simulation with the EFDM is taken as the "exact" solution in order to calculate the errors in all five models (see Appendix D).

$\Delta x = \Delta y = 125$ m, we can see from Fig. 9 that $\|\Delta\zeta\|_\infty$ for the SSM ($\approx 1.04 \times 10^{-5}$ s^{-1}) is about four times larger than $\|\Delta\zeta\|_\infty$ for the BVEM ($\approx 2.60 \times 10^{-6}$ s^{-1}). The ζ error norms for the SSM are larger than those for the BVEM despite the fact that the convergence rates of $\|\Delta\zeta\|_2$ and $\|\Delta\zeta\|_\infty$ for the SSM (which are 1.25 and 1–1.25, respectively; see Table 1) are slightly higher than those for the BVEM (with rates of 1–1.25 and 0.75). As we can see in Fig. 9, this is because the SSM error norms start out with larger values on the coarsest grid. Note also that as Δx and Δy are reduced, $\|\Delta\zeta\|_1$ and $\|\Delta\zeta\|_2$ for the SSM merge from above with $\|\Delta\zeta\|_1$ and $\|\Delta\zeta\|_2$ for the BVEM. Thus, the convergence rates of $\|\Delta\zeta\|_1$ and $\|\Delta\zeta\|_2$ are very likely the same for these two models in the limit as the grid spacing goes to zero. We suspect that the $\|\Delta\zeta\|_\infty$ values for these two models may also

merge in this limit (and thus their convergence rates become identical) because both models are formally first-order accurate in Δx and Δy. [The truncation errors in the boundary vorticity equations used by the BVEM (Appendix A) are first-order in Δx and Δy, and the super-slip boundary condition used by the SSM is just an extrapolation of the vorticity from within the fluid to the boundaries with error that is first-order in Δx and Δy.]

The behaviors of $\|\Delta\zeta\|_1'$, $\|\Delta\zeta\|_2'$, and $\|\Delta\zeta\|_\infty'$ (i.e. the L_1', L_2', and L_∞' error norms of ζ) for the BVEM, FSM, and SSM are more straightforward. As above, the FSM generates both larger magnitudes and smaller convergence rates than the BVEM and SSM for these error norms. Thus, it does not perform as well as the BVEM or SSM with respect to these error norms. The magnitudes and convergence rates of $\|\Delta\zeta\|_1'$ and $\|\Delta\zeta\|_2'$ are almost identical for the BVEM and SSM, and the convergence rates of $\|\Delta\zeta\|_\infty'$ for these two models are also about the same. However, the BVEM almost always produces smaller magnitudes for $\|\Delta\zeta\|_\infty'$ than does the SSM.

In summary, in the GRSs of ANU_Cart, all six error norms of ζ for the BVEM are less than or equal to those for the SSM, which are in turn always less than those for the FSM. Also, all six error norms of h, u, and v are almost identical for the BVEM, SSM, and FSM. Finally, many or all of the error norms for the EFDM and NSM fail to converge, and in some cases they diverge. Based on these results, we conclude that in the GRSs of ANU_Cart, the BVEM is the most accurate model, followed in order of decreasing accuracy by the SSM, the FSM, and the NSM and/or EFDM.

In light of the results of the conservation test in Section 8.1 and the grid refinement studies performed so far in this section, it is clear that the BVEM provides the best overall results. In the conservation test, it is the only model that conserves all four domain-summed quantities. It is also the only model that simultaneously prevents a spurious energy cascade to the small scales and maintains an overall flow pattern that is in the direction of the forcing. In the GRSs of axisymmetric flow in an annulus in Cartesian coordinates (ANU_Cart), it generates error norms of ζ that are the smallest of the five models, and it generates error norms of h, u, and v that are practically identical to the ones generated by the FSM and SSM (while the EFDM and NSM generate errors that do not converge and sometimes even diverge). Finally, in the GRSs of axisymmetric flow in an annulus in cylindrical coordinates (ANU_cyln), the BVEM generates results that are as or more accurate than all the other models except the EFDM. The only difference between the BVEM and EFDM in the GRSs of ANU_cyln is that the EFDM has a convergence rate of 2 for $\|\Delta\zeta\|_\infty$ while the BVEM has a rate of 1.1. Recall, however, that the EFDM fails to even converge in the GRSs of ANU_Cart; thus, it is not useful in the general case in which fluid–land boundaries are not exactly aligned with the model grid lines.

A clear trend in Table 1 is the reduction in convergence rates for the BVEM, FSM, and SSM as we go from cylindrical to Cartesian coordinates. As stated earlier, this is due to the presence of geometric errors in the GRSs of ANU_Cart, i.e. it is due to the fact that the model boundary in Cartesian coordinates is shifting as the grid is refined. Note from Table 1 that for all three models, the L_∞ error norms of h, u, and v do not converge. This is expected because the model boundary is always a stair-step. As a result, at or near the boundary the deviation from the exact solution (in which the boundary is circular) will always be large, i.e. if we "zoom-in" sufficiently to the model boundary, the solution there will look like flow around stair-steps; it will not look like flow around a smooth circle. This will be the case regardless of the grid spacing. The behavior of the L_∞ error norm (defined as the maximum absolute value of the error; see Appendix D) is indicating the presence of this error at or near the boundary. On the other hand, away from boundaries, the convergence is much improved, as seen by the 1–1.25 or 1.5 convergence rates of the L_1', L_2', and L_∞' error norms of h, u, and v.

In order to verify that the convergence rates obtained in the GRS of ANU_Cart with the BVEM can be reproduced in other flow configurations – especially configurations that are truly 2D in the sense that they cannot be reduced to a 1D problem in a different coordinate system – we now perform a final GRS with the BVEM of a flow in which a rotating core of positive vorticity is advected around an elliptic island (VCOR_ISL). The simulations in this GRS are in Cartesian coordinates with periodic boundary conditions in both x and y along the edges of the 20 km $\times$ 20 km domain. The island geometry and initial vorticity field are shown in Fig. 10a. The expressions for the initial conditions and forcing for this set of simulations are similar to the ones for the conservation test in Section 8.1, so we do not give them here. We integrate the model to $t = 50{,}000$ s ≈ 0.58 d using RK4, and we use grids with the following numbers of grid points in x and y: 40×40, 80×80, 160×160, 320×320, 640×640, and 1280×1280. Due to computer memory constraints, we do not use grids any finer than 1280×1280. The corresponding time steps are 20, 20, 10, 5, 4, and 2 s. The grid size is $\Delta x = \Delta y = 500$ m on the coarsest grid and 15.625 m on the finest. Note that, as in the GRSs of ANU_Cart, in this GRS the model boundaries shift as we move from coarser to finer grids in order to better approximate the elliptic boundary. As discussed in Appendix D, with a shifting boundary we cannot calculate the L_1, L_2, and L_∞ error norms of h, u, v, and ζ and must instead calculate the L_1', L_2', and L_∞' error norms. In calculating these, we take the simulation on the 1280×1280 grid as the "exact" solution.

Fig. 10 shows plots of the vorticity on the 1280×1280 grid at the beginning and end of the simulation. The vorticity core is initially advected toward the island by a uniform westerly forcing and subsequently gets stretched around the top of it. This flow is a thorough test of the boundary formulation because the vorticity core interacts heavily with the island's boundary. To assess the accuracy of the model, we plot the L_1', L_2', and L_∞' error norms of h, u, v, and ζ at every 2000 s. As an example, we show in Fig. 11 the L_1', L_2', and L_∞' error norms of u at the final time of $t = 50{,}000$ s. We can see from this figure that $\|\Delta u\|_1'$, $\|\Delta u\|_2'$, and $\|\Delta u\|_\infty'$ all have rates of convergence of about 1.5. Similar plots for h, v, and ζ indicate that the L_1', L_2', and L_∞' error norms of h and v at 50,000 s also converge at a rate of about 1.5 while those of ζ converge at a rate of about 1. These convergence rates are representative (to within ±0.25) of the rates between 40,000 and 50,000 s, which is the period in which the vorticity core interacts most heavily with the boundary. Before 40,000 s, the convergence rates are generally higher because the core has not yet fully interacted with the boundary (and thus the accuracy of the simulations is closer to that of the

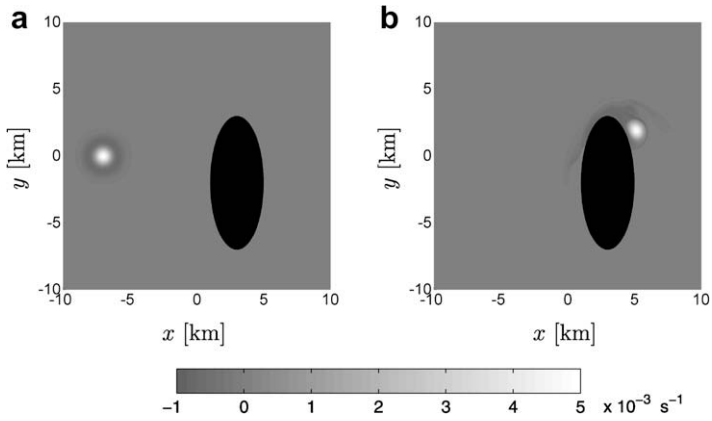

Fig. 10. Vorticity field on the 1280 × 1280 grid at (a) $t = 0$ s and (b) $t = 50{,}000$ s ≈ 0.58 d for the grid resolution study of advection of a core of vorticity around an elliptic island in Cartesian coordinates (VCOR_ISL) with the BVEM. The black regions are land, and both plots use the same gray scale for the vorticity. For plotting purposes, ζ has been averaged from ζ-points to h-points.

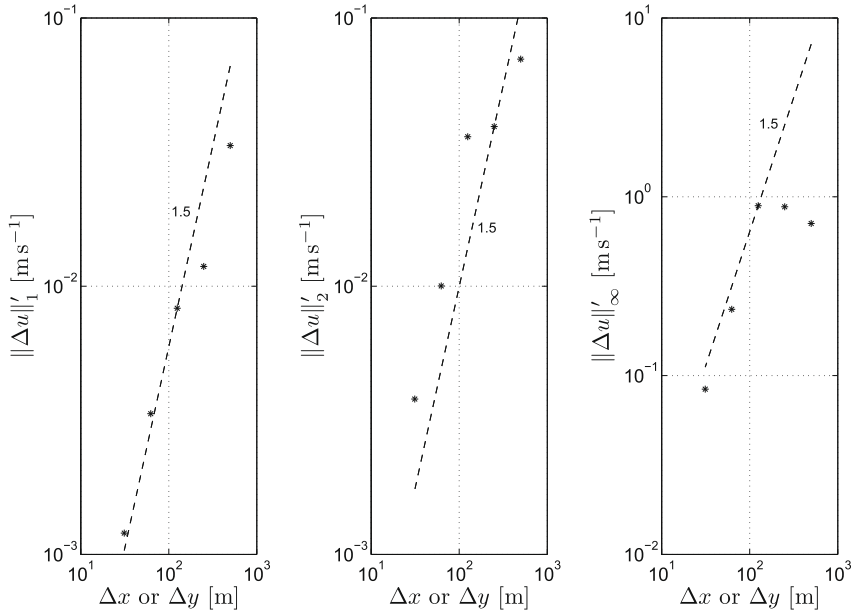

Fig. 11. L'_1, L'_2, and L'_∞ error norms of u at $t = 50{,}000$ s from the grid refinement study of advection of a core of vorticity around an elliptic island in Cartesian coordinates (VCOR_ISL) with the BVEM. The dashed lines are reference lines having the indicated slopes. The solution from the 1280 × 1280 simulation is taken as the "exact" solution in order to calculate the errors (see Appendix D).

AL81 scheme without land, which is second-order). Since the convergence rates for this flow are similar to those listed in Table 1, we conclude that the accuracy results obtained in the GRS of ANU_Cart with the BVEM are valid for general flows.

9. Conclusion

We have derived a new boundary scheme that allows the mass, energy, vorticity, and potential enstrophy conserving scheme of Arakawa and Lamb [4] for the inviscid shallow water equations to be implemented in domains with arbitrarily shaped boundaries, e.g. in domains with embedded islands, while maintaining all four conservation properties. We are concerned with arbitrarily shaped fluid–land boundaries because these are encountered in ocean models and in atmospheric models that use vertical coordinates that intersect the topography.

In our boundary scheme, we denote each h-point control volume (i.e. each grid box) as consisting of either entirely fluid or entirely land (a stair-step approach). To enforce the no-flux condition, we set the velocity components on control volume faces shared by a fluid and a land h-point to zero. This ensures conservation of domain-summed mass and energy. To

conserve domain-summed vorticity and potential enstrophy, we use specially formulated evolution equations for the vorticity and extrapolation formulas for the depth in order to obtain these two quantities at ζ-points (i.e. grid-box corners) that lie on boundaries. We then calculate the potential vorticity at such ζ-points by dividing the vorticity by the depth.

We ran numerical simulations demonstrating the conservation properties and accuracy of the new boundary scheme and comparing its performance with those of four alternative schemes for treating the boundaries. The latter consisted of the extrapolation/finite-differencing, the free-slip, the super-slip, and the no-slip schemes. The only difference between the five schemes is the way in which the vorticity at boundaries is calculated. Also, all five schemes conserve domain-summed mass and energy. Out of the five, we found that the new scheme gives the best results in terms of both conservation and accuracy. In the (long-term) conservation test, it was the only one of the five that conserved all four domain-summed quantities (i.e. mass, energy, vorticity, and potential enstrophy). It was also the only one that simultaneously prevented a spurious energy cascade to the small scales and maintained an overall flow orientation that was in the direction of the forcing. In the (short-term) accuracy tests, it generated vorticity fields that had smaller errors than the fields generated by the most accurate alternative scheme, and it generated depth and velocity fields that had errors about equal to those in the fields generated by the most accurate alternative scheme(s). The only exception to this was in the grid refinement study of axisymmetric flow in an annulus in cylindrical coordinates. In that study, the L_∞ error norm of the vorticity generated by the new scheme did not converge as quickly as the one generated by the extrapolation/finite-differencing scheme (rate of 1.1 vs. 2). However, this was negated by the fact that the extrapolation/finite-differencing scheme completely failed in the grid refinement study of axisymmetric flow in an annulus in Cartesian coordinates.

It is not too surprising that the four alternative boundary schemes do not perform so well as the new scheme derived in this paper. This is because in an inviscid model, the only physically meaningful condition that must be enforced at boundaries is the no-flux condition. Any additional boundary conditions are extraneous in the sense that they are not mathematically needed or physically justified. As pointed out in Section 6, in the inviscid SWEs, the vorticity at boundaries is a time-dependent quantity with a corresponding evolution equation. Thus, just as we do for the fluid depth and velocity components at points inside the fluid, the correct procedure for obtaining the vorticity at boundaries is to solve the proper evolution equation for it.

Acknowledgements

This research was supported by the National Science Foundation and the National Aeronautics and Space Administration. We would like to thank two anonymous reviewers for their valuable comments and suggestions.

Appendix A. Summary of boundary scheme

Here, we list the discrete vorticity equation, the expression for $h^{(q)}$, and the area associated with the ζ-point CV for each of the 12 possible boundary ζ-point fluid–land configurations:

- Concave corner, fluid to the northwest:

$$\frac{\mathrm{d}}{\mathrm{d}t}\left(A^{(\zeta)}\zeta\right)_{i+1/2,j+1/2} = F^{(\zeta),\mathrm{NW}}_{i+1/2,j+1/2} - G^{(\zeta),\mathrm{NW}}_{i+1/2,j+1/2} \tag{A.1}$$

$$h^{(q)}_{i+1/2,j+1/2} = \frac{\Pi_{i,j+1}}{4A^{(\zeta)}_{i+1/2,j+1/2}} \tag{A.2}$$

$$A^{(\zeta)}_{i+1/2,j+1/2} = A^{(\zeta),\mathrm{NW}}_{i+1/2,j+1/2} \tag{A.3}$$

- Concave corner, fluid to the northeast:

$$\frac{\mathrm{d}}{\mathrm{d}t}\left(A^{(\zeta)}\zeta\right)_{i+1/2,j+1/2} = -F^{(\zeta),\mathrm{NE}}_{i+1/2,j+1/2} - G^{(\zeta),\mathrm{NE}}_{i+1/2,j+1/2} \tag{A.4}$$

$$h^{(q)}_{i+1/2,j+1/2} = \frac{\Pi_{i+1,j+1}}{4A^{(\zeta)}_{i+1/2,j+1/2}} \tag{A.5}$$

$$A^{(\zeta)}_{i+1/2,j+1/2} = A^{(\zeta),\mathrm{NE}}_{i+1/2,j+1/2} \tag{A.6}$$

- Concave corner, fluid to the southwest:

$$\frac{\mathrm{d}}{\mathrm{d}t}\left(A^{(\zeta)}\zeta\right)_{i+1/2,j+1/2} = F^{(\zeta),\mathrm{SW}}_{i+1/2,j+1/2} + G^{(\zeta),\mathrm{SW}}_{i+1/2,j+1/2} \tag{A.7}$$

$$h^{(q)}_{i+1/2,j+1/2} = \frac{\Pi_{i,j}}{4A^{(\zeta)}_{i+1/2,j+1/2}} \tag{A.8}$$

$$A^{(\zeta)}_{i+1/2,j+1/2} = A^{(\zeta),\mathrm{SW}}_{i+1/2,j+1/2} \tag{A.9}$$

- Concave corner, fluid to the southeast:

$$\frac{\mathrm{d}}{\mathrm{d}t}(A^{(\zeta)}\zeta)_{i+1/2,j+1/2} = -F^{(\zeta),\mathrm{SE}}_{i+1/2,j+1/2} + G^{(\zeta),\mathrm{SE}}_{i+1/2,j+1/2} \tag{A.10}$$

$$h^{(q)}_{i+1/2,j+1/2} = \frac{\Pi_{i+1,j}}{4A^{(\zeta)}_{i+1/2,j+1/2}} \tag{A.11}$$

$$A^{(\zeta)}_{i+1/2,j+1/2} = A^{(\zeta),\mathrm{SE}}_{i+1/2,j+1/2} \tag{A.12}$$

- Horizontal wall, fluid to the north:

$$\frac{\mathrm{d}}{\mathrm{d}t}(A^{(\zeta)}\zeta)_{i+1/2,j+1/2} = -(F^{(\zeta),\mathrm{NE}}_{i+1/2,j+1/2} - F^{(\zeta),\mathrm{NW}}_{i+1/2,j+1/2}) - G^{(\zeta)}_{i+1/2,j+1} \tag{A.13}$$

$$h^{(q)}_{i+1/2,j+1/2} = \frac{\overline{\Pi}^{\xi}_{i+1/2,j+1}}{2A^{(\zeta)}_{i+1/2,j+1/2}} \tag{A.14}$$

$$A^{(\zeta)}_{i+1/2,j+1/2} = (A^{(\zeta),\mathrm{NW}} + A^{(\zeta),\mathrm{NE}})_{i+1/2,j+1/2} \tag{A.15}$$

- Horizontal wall, fluid to the south:

$$\frac{\mathrm{d}}{\mathrm{d}t}(A^{(\zeta)}\zeta)_{i+1/2,j+1/2} = -(F^{(\zeta),\mathrm{SE}}_{i+1/2,j+1/2} - F^{(\zeta),\mathrm{SW}}_{i+1/2,j+1/2}) + G^{(\zeta)}_{i+1/2,j} \tag{A.16}$$

$$h^{(q)}_{i+1/2,j+1/2} = \frac{\overline{\Pi}^{\xi}_{i+1/2,j}}{2A^{(\zeta)}_{i+1/2,j+1/2}} \tag{A.17}$$

$$A^{(\zeta)}_{i+1/2,j+1/2} = (A^{(\zeta),\mathrm{SW}} + A^{(\zeta),\mathrm{SE}})_{i+1/2,j+1/2} \tag{A.18}$$

- Vertical wall, fluid to the west:

$$\frac{\mathrm{d}}{\mathrm{d}t}(A^{(\zeta)}\zeta)_{i+1/2,j+1/2} = -F^{(\zeta)}_{i+1,j+1/2} - (G^{(\zeta),\mathrm{NE}}_{i+1/2,j+1/2} - G^{(\zeta),\mathrm{SE}}_{i+1/2,j+1/2}) \tag{A.19}$$

$$h^{(q)}_{i+1/2,j+1/2} = \frac{\overline{\Pi}^{\eta}_{i+1,j+1/2}}{2A^{(\zeta)}_{i+1/2,j+1/2}} \tag{A.20}$$

$$A^{(\zeta)}_{i+1/2,j+1/2} = (A^{(\zeta),\mathrm{NE}} + A^{(\zeta),\mathrm{SE}})_{i+1/2,j+1/2} \tag{A.21}$$

- Vertical wall, fluid to the east:

$$\frac{\mathrm{d}}{\mathrm{d}t}(A^{(\zeta)}\zeta)_{i+1/2,j+1/2} = F^{(\zeta)}_{i,j+1/2} - (G^{(\zeta),\mathrm{NW}}_{i+1/2,j+1/2} - G^{(\zeta),\mathrm{SW}}_{i+1/2,j+1/2}) \tag{A.22}$$

$$h^{(q)}_{i+1/2,j+1/2} = \frac{\overline{\Pi}^{\eta}_{i,j+1/2}}{2A^{(\zeta)}_{i+1/2,j+1/2}} \tag{A.23}$$

$$A^{(\zeta)}_{i+1/2,j+1/2} = (A^{(\zeta),\mathrm{NW}} + A^{(\zeta),\mathrm{SW}})_{i+1/2,j+1/2} \tag{A.24}$$

- Convex corner, land to the southeast:

$$\frac{\mathrm{d}}{\mathrm{d}t}(A^{(\zeta)}\zeta)_{i+1/2,j+1/2} = -(F^{(\zeta),\mathrm{NE}}_{i+1/2,j+1/2} - F^{(\zeta)}_{i,j+1/2}) - (G^{(\zeta)}_{i+1/2,j+1} - G^{(\zeta),\mathrm{SW}}_{i+1/2,j+1/2}) \tag{A.25}$$

$$h^{(q)}_{i+1/2,j+1/2} = \frac{\Pi_{i,j+1} + \Pi_{i+1,j+1} + \Pi_{i,j}}{4A^{(\zeta)}_{i+1/2,j+1/2}} \tag{A.26}$$

$$A^{(\zeta)}_{i+1/2,j+1/2} = (A^{(\zeta),\mathrm{NW}} + A^{(\zeta),\mathrm{NE}} + A^{(\zeta),\mathrm{SW}})_{i+1/2,j+1/2} \tag{A.27}$$

- Convex corner, land to the southwest:

$$\frac{\mathrm{d}}{\mathrm{d}t}(A^{(\zeta)}\zeta)_{i+1/2,j+1/2} = -(F^{(\zeta)}_{i+1,j+1/2} - F^{(\zeta),\mathrm{NW}}_{i+1/2,j+1/2}) - (G^{(\zeta)}_{i+1/2,j+1} - G^{(\zeta),\mathrm{SE}}_{i+1/2,j+1/2}) \tag{A.28}$$

$$h^{(q)}_{i+1/2,j+1/2} = \frac{\Pi_{i,j+1} + \Pi_{i+1,j+1} + \Pi_{i+1,j}}{4A^{(\zeta)}_{i+1/2,j+1/2}} \tag{A.29}$$

$$A^{(\zeta)}_{i+1/2,j+1/2} = (A^{(\zeta),\mathrm{NW}} + A^{(\zeta),\mathrm{NE}} + A^{(\zeta),\mathrm{SE}})_{i+1/2,j+1/2} \tag{A.30}$$

- Convex corner, land to the northeast:

$$\frac{\mathrm{d}}{\mathrm{d}t}(A^{(\zeta)}\zeta)_{i+1/2,j+1/2} = -(F^{(\zeta),\mathrm{SE}}_{i+1/2,j+1/2} - F^{(\zeta)}_{i,j+1/2}) - (G^{(\zeta),\mathrm{NW}}_{i+1/2,j+1/2} - G^{(\zeta)}_{i+1/2,j}) \tag{A.31}$$

$$h^{(q)}_{i+1/2,j+1/2} = \frac{\Pi_{i,j+1} + \Pi_{ij} + \Pi_{i+1,j}}{4A^{(\zeta)}_{i+1/2,j+1/2}} \tag{A.32}$$

$$A^{(\zeta)}_{i+1/2,j+1/2} = (A^{(\zeta),\mathrm{NW}} + A^{(\zeta),\mathrm{SW}} + A^{(\zeta),\mathrm{SE}})_{i+1/2,j+1/2} \tag{A.33}$$

- Convex corner, land to the northwest:

$$\frac{\mathrm{d}}{\mathrm{d}t}(A^{(\zeta)}\zeta)_{i+1/2,j+1/2} = -(F^{(\zeta)}_{i+1,j+1/2} - F^{(\zeta),\mathrm{SW}}_{i+1/2,j+1/2}) - (G^{(\zeta),\mathrm{NE}}_{i+1/2,j+1/2} - G^{(\zeta)}_{i+1/2,j}) \tag{A.34}$$

$$h^{(q)}_{i+1/2,j+1/2} = \frac{\Pi_{i+1,j+1} + \Pi_{ij} + \Pi_{i+1,j}}{4A^{(\zeta)}_{i+1/2,j+1/2}} \tag{A.35}$$

$$A^{(\zeta)}_{i+1/2,j+1/2} = (A^{(\zeta),\mathrm{NE}} + A^{(\zeta),\mathrm{SW}} + A^{(\zeta),\mathrm{SE}})_{i+1/2,j+1/2} \tag{A.36}$$

In the vorticity equations above, the vorticity fluxes $F^{(\zeta)}$, $G^{(\zeta)}$, $F^{(\zeta),\mathrm{NW}}$, and $F^{(\zeta),\mathrm{SW}}$ are given by (49), (50), (67) and (68), and the rest are given as follows:

$$F^{(\zeta),\mathrm{NE}}_{i+1/2,j+1/2} = \left[\overline{F}^{\xi}\left(\frac{1}{2}\bar{q}^{\xi\eta} - \frac{1}{12}(\delta_\eta \bar{q}^{\xi})\right)\right]_{i+1,j+1} - \frac{1}{24}(\delta_\eta G)_{i+1,j+1}(\delta_\xi q)_{i+1,j+1/2} \tag{A.37}$$

$$F^{(\zeta),\mathrm{SE}}_{i+1/2,j+1/2} = \left[\overline{F}^{\xi}\left(\frac{1}{2}\bar{q}^{\xi\eta} + \frac{1}{12}(\delta_\eta \bar{q}^{\xi})\right)\right]_{i+1,j} - \frac{1}{24}(\delta_\eta G)_{i+1,j}(\delta_\xi q)_{i+1,j+1/2} \tag{A.38}$$

$$G^{(\zeta),\mathrm{NW}}_{i+1/2,j+1/2} = \left[\overline{G}^{\eta}\left(\frac{1}{2}\bar{q}^{\xi\eta} + \frac{1}{12}(\delta_\xi \bar{q}^{\eta})\right)\right]_{i,j+1} - \frac{1}{24}(\delta_\xi F)_{i,j+1}(\delta_\eta q)_{i+1/2,j+1} \tag{A.39}$$

$$G^{(\zeta),\mathrm{NE}}_{i+1/2,j+1/2} = \left[\overline{G}^{\eta}\left(\frac{1}{2}\bar{q}^{\xi\eta} - \frac{1}{12}(\delta_\xi \bar{q}^{\eta})\right)\right]_{i+1,j+1} - \frac{1}{24}(\delta_\xi F)_{i+1,j+1}(\delta_\eta q)_{i+1/2,j+1} \tag{A.40}$$

$$G^{(\zeta),\mathrm{SW}}_{i+1/2,j+1/2} = \left[\overline{G}^{\eta}\left(\frac{1}{2}\bar{q}^{\xi\eta} + \frac{1}{12}(\delta_\xi \bar{q}^{\eta})\right)\right]_{i,j} - \frac{1}{24}(\delta_\xi F)_{i,j}(\delta_\eta q)_{i+1/2,j} \tag{A.41}$$

$$G^{(\zeta),\mathrm{SE}}_{i+1/2,j+1/2} = \left[\overline{G}^{\eta}\left(\frac{1}{2}\bar{q}^{\xi\eta} - \frac{1}{12}(\delta_\xi \bar{q}^{\eta})\right)\right]_{i+1,j} - \frac{1}{24}(\delta_\xi F)_{i+1,j}(\delta_\eta q)_{i+1/2,j} \tag{A.42}$$

Also, the area $A^{(\zeta),\mathrm{NW}}$ is given by (79), and $A^{(\zeta),\mathrm{NE}}$, $A^{(\zeta),\mathrm{SW}}$, and $A^{(\zeta),\mathrm{SE}}$ are given by

$$A^{(\zeta),\mathrm{NE}}_{i+1/2,j+1/2} = \frac{1}{4}A^{(h)}_{i+1,j+1} \tag{A.43}$$

$$A^{(\zeta),\mathrm{SW}}_{i+1/2,j+1/2} = \frac{1}{4}A^{(h)}_{ij} \tag{A.44}$$

$$A^{(\zeta),\mathrm{SE}}_{i+1/2,j+1/2} = \frac{1}{4}A^{(h)}_{i+1,j} \tag{A.45}$$

Appendix B. Descriptions of EFDM, FSM, SSM, and NSM

In the EFDM, we use extrapolation and finite-differencing to calculate the relative vorticity ζ_{rel} [given by (5)] at boundaries. At horizontal walls, we calculate ζ_{rel} by setting $\partial(v/n)/\partial\xi$ to zero and obtaining $\partial(u/m)/\partial\eta$ by fitting a quadratic function of η to u/m through its values at the three u-points nearest to the wall, taking the derivative of this quadratic with respect to η, and evaluating the resulting linear function of η at the wall. We use an analogous extrapolation procedure to obtain ζ_{rel} at vertical walls. At convex corners, we use the relative part of the right-hand side of (21), i.e.

$$(\zeta_{\mathrm{rel}})_{i+1/2,j+1/2} = \left[\frac{1}{A^{(\zeta)}}\{\delta_\xi(v\,\Delta s_\eta) - \delta_\eta(u\,\Delta s_\xi)\}\right]_{i+1/2,j+1/2} \tag{B.1}$$

Note that this is a finite-difference expression for ζ_{rel}. Finally, at concave corners, we simply set ζ_{rel} to zero.

In the FSM, we enforce the free-slip condition at boundaries [37]. This consists of setting the derivative normal to the boundary of the velocity component tangent to the boundary to zero. Since ζ_{rel} at boundaries can be expressed solely in terms of the normal derivative of the tangential velocity component, the free-slip condition implies zero relative vorticity at boundaries. Thus, in the FSM, we set ζ_{rel} at boundary ζ-points to zero. (Note that, strictly speaking, the term "free-slip" implies zero shear at the boundary only for viscous flows. This is because in such flows, the stress at the boundary is proportional to the product of a nonzero viscosity and the shear. On the other hand, in inviscid flows, the stress is always zero

regardless of the shear because the viscosity is zero. Nevertheless, here we use the term "free-slip" to mean zero normal shear, or, equivalently, zero relative vorticity at the boundary.)

In the SSM, we enforce the super-slip condition [37]. This consists of setting the derivative normal to the boundary of ζ_{rel} to zero. At ζ-points located on horizontal or vertical walls, we do this by setting ζ_{rel} to its value at the nearest fluid ζ-point. For example, at the boundary ζ-point at $(i+1/2, j+1/2)$ on the horizontal wall in Fig. 4b, we set ζ_{rel} to its value at $(i+1/2, j+3/2)$. The procedure for finding ζ_{rel} at convex and concave corners is more complex because it involves bilinear fitting. At convex corners, we assume ζ_{rel} has a bilinear functional form over the one neighboring fluid h-point CV that has three of its corners in fluid and the fourth at the convex corner. Recall that bilinear functions in 2D contain four coefficients. To determine these, we must impose four independent conditions. For three of these, we require that the bilinear function give the known values of ζ_{rel} at the three fluid corners of the h-point CV. [These known values are obtained by subtracting f from the expression for ζ given by (21), or, equivalently, by using (B.1).] For the fourth condition, we require that the derivative normal to the boundary of the bilinear function for ζ_{rel} be zero at the fourth corner of the h-point CV (i.e. at the convex corner in consideration). We take the direction normal to the boundary to be along the diagonal line that passes through the convex corner and the center of the h-point CV. Note that this line is at an angle $\pm\tan^{-1}(\Delta\eta/\Delta\xi)$ to the horizontal. We use these four conditions to determine the four coefficients in the bilinear function for ζ_{rel}. We then use this function to calculate ζ_{rel} at the convex corner. We use a similar procedure to obtain ζ_{rel} at concave corners.

Finally, in the NSM, we enforce the no-slip condition. This consists of setting the velocity component tangent to the boundary to zero. We use this condition to obtain ζ_{rel} at boundaries as follows. At horizontal walls, we calculate ζ_{rel} by setting $\partial(v/n)/\partial\xi$ to zero and obtaining $\partial(u/m)/\partial\eta$ by fitting a quadratic function of η to u/m through its values at the two u-points nearest to the wall and the no-slip condition $u/m = 0$ at the wall, taking the derivative of this quadratic with respect to η, and evaluating the resulting linear function of η at the wall. We use an analogous procedure to obtain ζ_{rel} at vertical walls. At convex corners, we use (B.1), and at concave corners, we simply set ζ_{rel} to zero. Note that the methods used to obtain ζ_{rel} at convex and concave corners are identical in the EFDM and NSM models.

Appendix C. Excluded fluid–land configurations

For coding convenience, we exclude from the model fluid–land configurations in which exactly two of the four h-point CVs around a ζ-point are land and are positioned diagonally from each other (while the remaining two are fluid and are also positioned diagonally from each other). There are two such configurations; they are shown in Fig. 2. These complicate the computer code because they require two values of any physical quantity (e.g. the vorticity ζ or the depth $h^{(q)}$) at the ζ-point. One value is associated with the flow in one of the fluid h-point CVs and the other is associated with the flow in the other. Two values are required because the flows in the two fluid CVs are not directly connected and thus do not share the same boundary value.

If one or both of these configurations are encountered while trying to represent an arbitrary distribution of fluid and land on the model grid, the preferred remedy is to increase the model resolution so that the diagonal land strips that such configurations represent are better resolved. If this is not possible, one or both of the two fluid h-point CVs in such configurations must be reset to land, or one or both of the land h-point CVs must be reset to fluid. Note that this is not an issue in the numerical simulations presented in this paper because in these, the two excluded configurations are never encountered.

We emphasize here that there is no fundamental obstacle to including these two fluid–land configurations in the model; we have excluded them only for convenience. We can obtain both sets of quantities at the double-valued ζ-points associated with these configurations using the appropriate equations and formulas from Appendix A. For example, to obtain the values of ζ and $h^{(q)}$ associated with the flow to the northeast of the ζ-point in Fig. 2a [which are needed to calculate the right-hand side of the u equation (16) at $(i+3/2, j+1)$ and the right-hand side of the v equation (17) at $(i+1, j+3/2)$], we treat the ζ-point as if it were located at a concave corner with fluid only to its northeast. We can then use (A.4)–(A.6) to obtain ζ and $h^{(q)}$. To obtain the values of ζ and $h^{(q)}$ associated with the flow to the southwest of this same ζ-point, we use (A.7)–(A.9). Similarly, to obtain the values of ζ and $h^{(q)}$ associated with the flow to the northwest of the ζ-point in Fig. 2b, we use (A.1)–(A.3), and to obtain the values associated with the flow to the southeast, we use (A.10)–(A.12). This treatment of double-valued ζ-points maintains all four conservation properties of the boundary scheme.

Appendix D. Calculation of error norms

In Section 8.2, we present results from grid refinement studies (GRSs) of axisymmetric flow in an annulus in both cylindrical (ANU_cyln) and Cartesian (ANU_Cart) coordinates and a GRS of advection of a core of vorticity around an elliptic island in Cartesian coordinates (VCOR_ISL). We then analyze the behaviors of the L_1, L_2, and L_∞ and/or the L_1', L_2', and L_∞' error norms of h, u_ξ, u_η, and ζ as the grid is refined in order to assess the accuracies of the various boundary models (i.e. the BVEM, EFDM, FSM, SSM, and NSM). In this appendix, we present the definitions of these error norms and the methods used to calculate them.

Given an approximate scalar field $\phi(\xi,\eta)$ and its exact counterpart $\phi^{(e)}(\xi,\eta)$, we define the error $\Delta\phi$ in ϕ as follows:

$$\Delta\phi = \phi - \phi^{(e)} \tag{D.1}$$

The L_1, L_2, and L_∞ norms of $\Delta\phi$ are given by

$$\|\Delta\phi\|_1 = \frac{1}{A}\int_\Omega |\Delta\phi| \mathrm{d}s_\xi \, \mathrm{d}s_\eta = \frac{1}{A}\int_\Omega |\Delta\phi| \mathrm{d}A \tag{D.2}$$

$$\|\Delta\phi\|_2 = \left[\frac{1}{A}\int_\Omega |\Delta\phi|^2 \, \mathrm{d}s_\xi \, \mathrm{d}s_\eta\right]^{1/2} = \left[\frac{1}{A}\int_\Omega |\Delta\phi|^2 \, \mathrm{d}A\right]^{1/2} \tag{D.3}$$

$$\|\Delta\phi\|_\infty = \max_{(\xi,\eta)\in\Omega} |\Delta\phi| \tag{D.4}$$

Recall from Section 2 that Ω is the flow domain in the $\xi\eta$ plane (not including land bodies), and $\mathrm{d}s_\xi = \mathrm{d}\xi/m$ and $\mathrm{d}s_\eta = \mathrm{d}\eta/n$ are incremental physical distances along curves of constant η and ξ, respectively. In (D.2) and (D.3), A denotes the physical area of Ω, and $\mathrm{d}A = \mathrm{d}s_\xi \, \mathrm{d}s_\eta$ is an infinitesimal portion of A. Thus, A is given by

$$A = \int_\Omega \mathrm{d}A = \int_\Omega \mathrm{d}s_\xi \, \mathrm{d}s_\eta = \int_\Omega \frac{\mathrm{d}\xi}{m}\frac{\mathrm{d}\eta}{n} \tag{D.5}$$

We discretize (D.2)–(D.4) over h-point CVs as follows:

$$\|\Delta\phi\|_1 = \frac{1}{A}\sum_{\substack{\text{fluid}\\ h\text{-points}}} |(\Delta\phi)_{i,j}| A_{i,j}^{(h)} \tag{D.6}$$

$$\|\Delta\phi\|_2 = \left[\frac{1}{A}\sum_{\substack{\text{fluid}\\ h\text{-points}}} |(\Delta\phi)_{i,j}|^2 A_{i,j}^{(h)}\right]^{1/2} \tag{D.7}$$

$$\|\Delta\phi\|_\infty = \max_{\substack{\text{fluid}\\ h\text{-points}}} |(\Delta\phi)_{i,j}| \tag{D.8}$$

We calculate the total fluid area A appearing in (D.6) and (D.7) using the following discrete counterpart of (D.5):

$$A = \sum_{\substack{\text{fluid}\\ h\text{-points}}} A_{i,j}^{(h)} \tag{D.9}$$

In these expressions, $A_{i,j}^{(h)}$ given by (15) is the physical area of the h-point CV at (i,j), and $(\Delta\phi)_{i,j}$ is the error in ϕ evaluated at the center of this CV. The way $(\Delta\phi)_{i,j}$ is calculated depends on the quantity that ϕ represents. Here, we are interested in the case of ϕ representing h, u_ξ, u_η, or ζ. We calculate the errors in these four quantities as follows:

$$(\Delta h)_{i,j} = h_{i,j} - (h^{(e)})_{i,j} \tag{D.10}$$

$$(\Delta u_\xi)_{i,j} = \overline{(u_\xi)}^{\xi}_{i,j} - (u_\xi^{(e)})_{i,j} \tag{D.11}$$

$$(\Delta u_\eta)_{i,j} = \overline{(u_\eta)}^{\eta}_{i,j} - (u_\eta^{(e)})_{i,j} \tag{D.12}$$

$$(\Delta\zeta)_{i,j} = \overline{\zeta}^{\xi\eta}_{i,j} - (\zeta^{(e)})_{i,j} \tag{D.13}$$

In these, $(h^{(e)})_{i,j}$, $(u_\xi^{(e)})_{i,j}$, $(u_\eta^{(e)})_{i,j}$, and $(\zeta^{(e)})_{i,j}$ denote the exact values of h, u_ξ, u_η, and ζ at the center of the CV at (i,j) [or, more briefly, at (i,j)]. Note that we do not have analytic solutions to any of the flows simulated in Section 8.2. Thus, we must somehow approximate the exact values in (D.10)–(D.13). We describe this procedure below.

Given a set of simulations on successively finer grids, we in general obtain an approximation to the exact solution (which we will refer to as the "exact" solution) using the solution on the finest grid. This is the approach we use in the GRSs of ANU_cyln and VCOR_ISL in Section 8.2. (Note that we would normally also use this approach in the GRSs of ANU_Cart, but it turns out that we can obtain a much better approximation to the exact solution in this case by using the solution from the finest-grid simulation in cylindrical coordinates with the EFDM. We discuss this in more detail later below.) More specifically, we calculate the "exact" value of a quantity at (i,j) on a given coarser grid by taking the average of its values at those h-point CVs on the finest grid that lie inside the coarser-grid h-point CV at (i,j). Thus, we have

$$(h^{(e)})_{i,j} = \frac{1}{N_\xi N_\eta} \times \sum_{i'=i'_{\min}(i)}^{i'_{\max}(i)} \sum_{j'=j'_{\min}(j)}^{j'_{\max}(j)} h^*_{i',j'} \tag{D.14}$$

$$(u_\xi^{(e)})_{i,j} = \frac{1}{N_\xi N_\eta} \times \sum_{i'=i'_{\min}(i)}^{i'_{\max}(i)} \sum_{j'=j'_{\min}(j)}^{j'_{\max}(j)} \overline{(u^*_\xi)}^{\xi}_{i',j'} \tag{D.15}$$

$$(u_\eta^{(e)})_{i,j} = \frac{1}{N_\xi N_\eta} \times \sum_{i'=i'_{\min}(i)}^{i'_{\max}(i)} \sum_{j'=j'_{\min}(j)}^{j'_{\max}(j)} \overline{(u^*_\eta)}^{\eta}_{i',j'} \tag{D.16}$$

$$(\zeta^{(e)})_{i,j} = \frac{1}{N_\xi N_\eta} \times \sum_{i'=i'_{\min}(i)}^{i'_{\max}(i)} \sum_{j'=j'_{\min}(j)}^{j'_{\max}(j)} \overline{(\zeta^*)}^{\xi\eta}_{i',j'} \tag{D.17}$$

where the starred quantities represent the solution on the finest grid and the summation limits are given by

$$i'_{\min}(i) = N_\xi(i-1)+1; \quad i'_{\max}(i) = N_\xi i \tag{D.18}$$

$$j'_{\min}(j) = N_\eta(j-1)+1; \quad j'_{\max}(j) = N_\eta j \tag{D.19}$$

In these, N_ξ is the number of h-point CVs in the ξ direction on the finest grid for every one such CV in the ξ direction on the coarser grid. N_η is defined in an analogous way. Thus, the product $N_\xi N_\eta$ appearing in (D.14)–(D.17) represents the number of finest-grid CVs that lie inside one coarser-grid CV. N_ξ and N_η are given by

$$N_\xi = \frac{I'}{I}; \quad N_\eta = \frac{J'}{J} \tag{D.20}$$

where I and J are the number of grid points in the ξ and η directions, respectively, on the coarser grid, and I' and J' are the corresponding values on the finest grid. (We assume here that I' and J' are integer multiples of I and J, respectively. This is always the case in the GRSs in Section 8.2.)

In order to use (D.14)–(D.17) to obtain the "exact" values of $h,\ u_\xi,\ u_\eta$, and ζ at (i,j), all the finest-grid h-point CVs inside the coarser-grid h-point CV at (i,j) must be fluid. This is because if some of these finest-grid CVs are land, some of the terms in the sums on the RHSs of (D.14)–(D.17) will be undefined (because the dependent variables are undefined within land). This requirement will always be satisfied at fluid h-point CVs that are not adjacent to fluid–land boundaries. (Here, we consider a CV to be adjacent to a boundary if one or more of its faces and/or corners lies on a boundary.) It will also be satisfied at fluid h-point CVs that are adjacent to a boundary – which we will refer to as boundary h-point CVs – if the model boundaries do not shift as the grid is refined, i.e. if the boundaries are represented exactly on all the grids. Recall from Section 8.2 that this is the case for the GRSs of ANU_cyln. Thus, we can (and do) use (D.6)–(D.20) to calculate the $L_1,\ L_2$, and L_∞ error norms for these GRSs. Note that we use the finest-grid solution with the EFDM for $h^*,\ u^*_\xi,\ u^*_\eta$, and ζ^* in (D.14)–(D.17) for all five models because in cylindrical coordinates (but not in Cartesian coordinates), the EFDM turns out to be the most accurate model.

If the model boundaries do shift as we move from coarser to finer grids (in order to better approximate the shapes of the exact boundaries), the requirement above that all the finest-grid h-point CVs inside a coarser-grid h-point CV be fluid will not be satisfied. This is because the fluid–land boundaries on the finest grid will cut through some or all of the boundary CVs on the coarser grids. As a result, some of the finest-grid CVs that lie inside these coarser-grid boundary CVs will be land, rendering the RHSs of (D.14)–(D.17) undefined at such coarser-grid CVs. Recall from Section 8.2 that in the GRS of VCOR_ISL, the model boundaries shift as the grid is refined. Thus, we cannot use (D.6)–(D.20) to calculate the $L_1,\ L_2$, and L_∞ error norms for this GRS. The most straightforward way to circumvent this difficulty is to use an alternate set of error norms – which we will refer to as the $L'_1,\ L'_2$, and L'_∞ norms – that, instead of spanning the whole fluid domain Ω, span a subdomain of Ω that does not encompass boundary CVs on any of the grids. Such a domain will necessarily exclude those parts of Ω that are near boundaries. This approach works because in such a subdomain, all h-point CVs will be away from boundaries; thus, we do not have to worry about obtaining "exact" values at boundary CVs. We will denote this subdomain by Ω' and its physical area by A'. We now define the modified $L'_1,\ L'_2$, and L'_∞ error norms as follows:

$$\|\Delta\phi\|'_1 = \frac{1}{A'}\int_{\Omega'} |\Delta\phi| \mathrm{d}s_\xi \,\mathrm{d}s_\eta = \frac{1}{A'}\int_{\Omega'} |\Delta\phi| \mathrm{d}A \tag{D.21}$$

$$\|\Delta\phi\|'_2 = \left[\frac{1}{A'}\int_{\Omega'} |\Delta\phi|^2 \mathrm{d}s_\xi \,\mathrm{d}s_\eta\right]^{1/2} = \left[\frac{1}{A'}\int_{\Omega'} |\Delta\phi|^2 \mathrm{d}A\right]^{1/2} \tag{D.22}$$

$$\|\Delta\phi\|'_\infty = \max_{(\xi,\eta)\in\Omega'} |\Delta\phi| \tag{D.23}$$

Here, A' is given by

$$A' = \int_{\Omega'} \mathrm{d}A = \int_{\Omega'} \mathrm{d}s_\xi \,\mathrm{d}s_\eta = \int_{\Omega'} \frac{\mathrm{d}\xi}{m}\frac{\mathrm{d}\eta}{n} \tag{D.24}$$

Note that the only difference between (D.2)–(D.5) and (D.21)–(D.24) is that Ω and A in the former are replaced with Ω' and A' in the latter. In analogy with (D.6)–(D.8), we discretize (D.21)–(D.23) as follows:

$$\|\Delta\phi\|'_1 = \frac{1}{A'}\sum_{\substack{\text{fluid } h\text{-pts} \\ \text{within } \Omega'}} |(\Delta\phi)_{i,j}| A^{(h)}_{i,j} \tag{D.25}$$

$$\|\Delta\phi\|'_2 = \left[\frac{1}{A'}\sum_{\substack{\text{fluid } h\text{-pts} \\ \text{within } \Omega'}} |(\Delta\phi)_{i,j}|^2 A^{(h)}_{i,j}\right]^{1/2} \tag{D.26}$$

$$\|\Delta\phi\|'_\infty = \max_{\substack{\text{fluid } h\text{-pts} \\ \text{within } \Omega'}} |(\Delta\phi)_{i,j}| \tag{D.27}$$

Also, in analogy with (D.9), we calculate the area A' using the following discrete counterpart of (D.24):

$$A' = \sum_{\substack{\text{fluid } h\text{-pts} \\ \text{within } \Omega'}} A_{i,j}^{(h)} \tag{D.28}$$

Of course, the drawback of using the L_1', L_2', and L_∞' error norms is that they do not include errors in regions of the flow domain near boundaries. In order to minimize this drawback, we would like Ω' to include as much of Ω as possible (without including boundary CVs on any of the grids). The choice of Ω' that has the greatest possible extent and that still allows us to calculate L_1', L_2', and L_∞' error norms on all the grids is the subdomain that remains after we remove all boundary CVs from the flow domain Ω on the coarsest grid. Thus, we will choose to define Ω' in this way. With Ω' now defined, we can (and do) use (D.25)–(D.28) along with (D.10)–(D.20) to calculate the L_1', L_2', and L_∞' error norms of h, u, v, and ζ in the GRS of VCOR_ISL.

Recall from Section 8.2 that as in the GRS of VCOR_ISL, in the GRSs of ANU_Cart the model boundaries shift as the grid is refined. Thus, normally, we would have to calculate the L_1', L_2', and L_∞' error norms for these GRSs. Fortunately, we do not have to; we can still calculate the L_1, L_2, and L_∞ error norms because we have available the highly resolved 10,240-point simulations of this geometry in cylindrical coordinates with all five models. These cylindrical simulations are much more resolved than even the 832×832 simulations on the finest Cartesian grid. Thus, we can use one of them instead of (D.14)–(D.17) to obtain "exact" values. We choose here to use the 10,240-point simulation with the EFDM because, as mentioned above, the EFDM turns out to be the most accurate model in cylindrical coordinates (but definitely not in Cartesian coordinates; see Section 8.2). The procedure we use is as follows. We first calculate the radial coordinate $r_{i,j}$ corresponding to the Cartesian coordinates (x_i, y_j) of the h-point at (i,j) on a given Cartesian grid. We then obtain an approximation to the exact value at this $r_{i,j}$ from the 10,240-point cylindrical simulation using linear interpolation between the two grid points on the cylindrical grid that bracket $r_{i,j}$. [Recall that since the flow is axisymmetric, the solution in cylindrical coordinates (r,θ) is not a function of θ.] In the calculations of the errors in the Cartesian velocity components u and v, we first use linear interpolation to obtain the "exact" cylindrical velocity components u_r and u_θ at $r_{i,j}$ and then use a cylindrical-to-Cartesian vector component transformation to obtain the "exact" Cartesian velocity components at $r_{i,j}$.

In summary, we use the L_1, L_2, and L_∞ error norms given by (D.6)–(D.8) for the GRSs of axisymmetric flow in an annulus, both in cylindrical and in Cartesian coordinates. For the GRSs in cylindrical coordinates, we calculate the "exact" values using (D.14)–(D.17), taking h^*, u_ξ^*, u_η^*, and ζ^* in these expressions to be the fields generated by the 10,240-point simulation with the EFDM (for all five models). For the GRSs in Cartesian coordinates, we calculate the "exact" values by linearly interpolating with the 10,240-point simulation in cylindrical coordinates with the EFDM. Note that although we do not have to, in Section 8.2 we also calculate the L_1', L_2', and L_∞' error norms for the GRSs of axisymmetric flow in an annulus, both in cylindrical and in Cartesian coordinates. We do this because differences between the two sets of error norms reveal the behavior of the error at and/or near the boundaries. We calculate the "exact" values in the L_1', L_2', and L_∞' error norms in exactly the same way as we do in the L_1, L_2, and L_∞ error norms, i.e. using the 10,240-point simulation in cylindrical coordinates with the EFDM. Finally, for the GRS of advection of a core of vorticity around an elliptic island in Cartesian coordinates, we have no choice but to calculate the L_1', L_2', and L_∞' error norms. We calculate the "exact" values in this case using (D.14)–(D.17), taking h^*, u_ξ^*, u_η^*, and ζ^* in these expressions to be the fields generated by the 1280×1280 simulation.

References

[1] A. Arakawa, Computational design for long-term numerical integration of the equations of fluid motion: two-dimensional incompressible flow. Part I, J. Comput. Phys. 1 (1966) 119–143.
[2] R. Sadourny, The dynamics of finite-difference models of the shallow-water equations, J. Atmos. Sci. 32 (1975) 680–689.
[3] A. Arakawa, V.R. Lamb, Computational design of the basic dynamical processes of the UCLA general circulation model, in: J. Chang (Ed.), General Circulation Models of the Atmosphere. Methods in Computational Physics: Advances in Research and Applications, vol. 17, Academic Press, 1977, pp. 173–265.
[4] A. Arakawa, V.R. Lamb, A potential enstrophy and energy conserving scheme for the shallow water equations, Mon. Weather Rev. 109 (1981) 18–36.
[5] K. Takano, M.G. Wurtele, A fourth order energy and potential enstrophy conserving difference scheme, Tech. Rep. AFGL-TR-82-0205 (NTIS AD-A126626), Air Force Geophysics Laboratory, Hanscom AFB, 1982.
[6] F. Abramopoulos, Generalized energy and potential enstrophy conserving finite difference schemes for the shallow water equations, Mon. Weather Rev. 116 (1988) 650–662.
[7] F. Abramopoulos, A new fourth-order enstrophy and energy conserving scheme, Mon. Weather Rev. 119 (1991) 128–133.
[8] G.J. Tripoli, A nonhydrostatic mesoscale model designed to simulate scale interaction, Mon. Weather Rev. 120 (1992) 1342–1359.
[9] Z.I. Janjić, Pressure gradient force and advection scheme used for forecasting with steep and small scale topography, Contrib. Atmos. Phys. 50 (1977) 186–199.
[10] F. Mesinger, Horizontal advection schemes of a staggered grid – an enstrophy and energy-conserving model, Mon. Weather Rev. 109 (1981) 467–478.
[11] Z.I. Janjić, Nonlinear advection schemes and energy cascade on semi-staggered grids, Mon. Weather Rev. 112 (1984) 1234–1245.
[12] M. Rančić, Fourth-order horizontal advection schemes on the semi-staggered grid, Mon. Weather Rev. 116 (1988) 1274–1288.
[13] R. Sadourny, A. Arakawa, Y. Mintz, Integration of the nondivergent barotropic vorticity equation with an icosahedral–hexagonal grid for the sphere, Mon. Weather Rev. 96 (1968) 351–356.
[14] R. Salmon, L.D. Talley, Generalizations of Arakawa's Jacobian, J. Comput. Phys. 83 (1989) 247–259.
[15] B. Perot, Conservation properties of unstructured staggered mesh schemes, J. Comput. Phys. 159 (2000) 58–89.
[16] K.W. Morton, P.L. Roe, Vorticity-preserving Lax–Wendroff-type schemes for the system wave equation, SIAM J. Sci. Comput. 23 (2001) 170–192.
[17] T.D. Ringler, D.A. Randall, A potential enstrophy and energy conserving numerical scheme for solution of the shallow-water equations on a geodesic grid, Mon. Weather Rev. 130 (2002) 1397–1410.
[18] T.D. Ringler, D.A. Randall, The ZM grid: an alternative to the Z grid, Mon. Weather Rev. 130 (2002) 1411–1422.

[19] L. Bonaventura, T. Ringler, Analysis of discrete shallow-water models on geodesic delauney grids with C-type staggering, Mon. Weather Rev. 133 (2005) 2351–2373.
[20] R. Salmon, Poisson-bracket approach to the construction of energy- and potential-enstrophy-conserving algorithms for the shallow-water equations, J. Atmos. Sci. 61 (2004) 2016–2036.
[21] R. Salmon, A general method for conserving quantities related to potential vorticity in numerical models, Nonlinearity 18 (2005) R1–R16.
[22] R. Salmon, A general method for conserving energy and potential enstrophy in shallow-water models, J. Atmos. Sci. 64 (2007) 515–531.
[23] F. Mesinger, Z.I. Janjić, S. Ničković, D. Gavrilov, D.G. Deaven, The step-mountain coordinate: model description and performance for cases of alpine lee cyclogenesis and for a case of an Appalachian redevelopment, Mon. Weather Rev. 116 (1988) 1493–1518.
[24] A. Adcroft, C. Hill, J. Marshall, Representation of topography by shaved cells in a height coordinate ocean model, Mon. Weather Rev. 125 (1997) 2293–2315.
[25] H.E. Hurlburt, J.D. Thompson, A numerical study of Loop Current intrusions and eddy shedding, J. Phys. Oceanogr. 10 (1980) 1611–1651.
[26] S. Jiang, F.-F. Jin, M. Ghil, Multiple equilibria, periodic, and aperiodic solutions in a wind-driven, double-gyre, shallow-water model, J. Phys. Oceanogr. 25 (1995) 764–786.
[27] H.A. Dijkstra, W.R.M. de Ruijter, On the physics of the Agulhas Current: steady retroflection regimes, J. Phys. Oceanogr. 31 (2001) 2971–2985.
[28] P. Sura, K. Fraedrich, F. Lunkeit, Regime transition in a stochastically forced double-gyre model, J. Phys. Oceanogr. 31 (2001) 411–426.
[29] E. Simonnet, M. Ghil, K. Ide, R. Temam, S. Wang, Low-frequency variability in shallow-water models of the wind-driven ocean circulation. Part I: Steady-state solution, J. Phys. Oceanogr. 33 (2003) 712–728.
[30] O. Marchal, J. Nycander, Nonuniform upwelling in a shallow-water model of the Antarctic bottom water in the Brazil Basin, J. Phys. Oceanogr. 34 (2004) 2492–2513.
[31] F.J. Poulin, G.R. Flierl, The influence of topography on the stability of jets, J. Phys. Oceanogr. 35 (2005) 811–825.
[32] T. Matsuura, M. Fujita, Two different aperiodic phases of wind-driven ocean circulation in a double-gyre, two-layer shallow-water model, J. Phys. Oceanogr. 36 (2006) 1265–1286.
[33] J.L. Evans, G.J. Holland, R.L. Elsberry, Interactions between a barotropic vortex and an idealized subtropical ridge. Part I: Vortex motion, J. Atmos. Sci. 48 (1991) 301–314.
[34] R.E. Hart, J.L. Evans, Simulations of dual-vortex interaction within environmental shear, J. Atmos. Sci. 56 (1999) 3605–3621.
[35] M.D. Mundt, G.K. Vallis, J. Wang, Balanced models and dynamics for the large- and mesoscale circulation, J. Phys. Oceanogr. 27 (1997) 1133–1152.
[36] G.S. Ketefian, Development and testing of a 2D potential enstrophy conserving ocean model and a 3D potential enstrophy conserving, nonhydrostatic, compressible atmospheric model, Ph.D. dissertation, Stanford University, 2006. <http://www.stanford.edu/group/efmh/gsk/ketefian_thesis.pdf>.
[37] G.F. Carnevale, F. Cavallini, F. Crisciani, Dynamic boundary conditions revisited, J. Phys. Oceanogr. 31 (2001) 2489–2497.
[38] F.W. Primeau, Multiple equilibria of a double-gyre ocean model with super-slip boundary conditions, J. Phys. Oceanogr. 28 (1998) 2130–2147.
[39] J. Wang, G.K. Vallis, Emergence of Fofonoff states in inviscid and viscous ocean circulation models, J. Mar. Res. 52 (1994) 83–127.
[40] R.J. Greatbatch, B.T. Nadiga, Four-gyre circulation in a barotropic model with double-gyre wind forcing, J. Phys. Oceanogr. 30 (2000) 1461–1471.
[41] A. Hollingsworth, P. Kallberg, V. Renner, D.M. Burridge, An internal symmetric computational instability, Quart. J. R. Meteor. Soc. 109 (1983) 417–428.